




Probing the Massive Star-forming Environment: A Multiwavelength Investigation of the Filamentary IRDC G333.73+0.37

V. S. Veena¹, S. Vig¹, B. Mookerjee², Á. Sánchez-Monge³ , A. Tej¹, and C. H. Ishwara-Chandra⁴

¹Indian Institute of Space Science and Technology, Thiruvananthapuram, 695 547, India

²Tata Institute of Fundamental Research, Mumbai, 600 005, India

³Physikalisches Institut, Universität zu Köln, Zùlpicher Str. 77, D-50937 Köln, Germany

⁴National Centre for Radio Astrophysics (NCRA-TIFR), Pune, 411 007, India

Received 2017 July 24; revised 2017 November 10; accepted 2017 November 13; published 2018 January 10

Abstract

We present a multiwavelength study of the filamentary infrared dark cloud (IRDC) G333.73+0.37. The region contains two distinct mid-infrared sources S1 and S2 connected by dark lanes of gas and dust. Cold dust emission from the IRDC is detected at seven wavelength bands, and we have identified 10 high-density clumps in the region. The physical properties of the clumps such as temperature (14.3–22.3 K) and mass (87–1530 M_{\odot}) are determined by fitting a modified blackbody to the spectral energy distribution of each clump between 160 μm and 1.2 mm. The total mass of the IRDC is estimated to be $\sim 4700 M_{\odot}$. The molecular line emission toward S1 reveals signatures of protostellar activity. Low-frequency radio emission at 1300 and 610 MHz is detected toward S1 (shell-like) and S2 (compact morphology), confirming the presence of newly formed massive stars in the IRDC. Photometric analysis of near- and mid-infrared point sources unveils the young stellar object population associated with the cloud. Fragmentation analysis indicates that the filament is supercritical. We observe a velocity gradient along the filament, which is likely to be associated with accretion flows within the filament rather than rotation. Based on various age estimates obtained for objects in different evolutionary stages, we attempt to set a limit to the current age of this cloud.

Key words: H II regions – infrared: ISM – infrared: stars – ISM: individual objects (G333.73+0.37) – radio continuum: ISM – stars: formation

1. Introduction

The formation of a massive star is believed to proceed along an evolutionary path that is at variance with that of the lower-mass counterparts, mainly due to the enhanced feedback mechanisms expected from the former. While theoretical formulations have been proposed to explain their formation (Zinnecker & Yorke 2007), observational studies of the early phases remain limited. The challenges are largely due to their rarity and short evolutionary timescales, in addition to obscuration produced by the associated molecular clouds. Possible clues to the earliest evolutionary phases of star formation can be found by examining dense clumps and cores nestled within infrared dark clouds (IRDCs). IRDCs are believed to be the progenitors of massive stars and star clusters, which are characterized by dark extinction features seen against the bright infrared Galactic background (Rathborne et al. 2006; Chambers et al. 2009). Initially detected by the Infrared Space Observatory (ISO) and then by the *Midcourse Space Experiment* (MSX; Perault et al. 1996; Egan et al. 1998), these massive clouds (10^2 – $10^4 M_{\odot}$) vary widely in their morphology from elongated to compact structures. On larger scales, IRDCs are associated with filamentary structures and sizes are seen to range from a few to hundreds of parsecs (Jackson et al. 2010; Ragan et al. 2014). Several works have revealed the properties of these filaments, such as the density structure, mass, stability, evolutionary stage, and kinematic properties (e.g., Henning et al. 2010; Miettinen 2012; Busquet et al. 2013; Beuther et al. 2015; Henshaw et al. 2016). In addition, recent studies suggest that large filaments extending up to 100 pc and beyond are likely to be the “bones” of the Milky Way (Goodman et al. 2014; Zucker et al. 2015). On smaller scales, they fragment into dense

clumps and cores (Battersby et al. 2010; Shipman et al. 2014; Zhang et al. 2017). IRDCs are dense ($n > 10^5 \text{ cm}^{-3}$), cold ($T < 20 \text{ K}$), and bright at submillimeter wavelengths (Carey et al. 2000). These extreme properties make them quintessential locales to forage for objects in the earliest phases in massive star formation.

Comprehensive analyses at far-infrared and submillimeter wavelengths show that IRDCs possess significant substructures within them that are undergoing a star formation flurry. Molecular line emission from these clumps and cores often exhibits signatures of protostellar activity such as infall and outflow (Beuther & Sridharan 2007; Jin et al. 2016), characterized by asymmetric line features. While some IRDCs harbor objects of different evolutionary stages such as maser spots, starless cores, ultracompact H II regions, and young stellar objects (YSOs), there are others that are devoid of any star formation activity (e.g., Beuther et al. 2013; Busquet et al. 2016). The latter serve as good targets to study the earliest phases prior to collapse, whereas those harboring H II regions and YSOs can be used to decipher the conditions under which the infant massive stars evolve. Thus, IRDCs can be broadly categorized on the basis of the evolutionary stage of the cloud itself. However, such a study necessitates a detailed scrutiny of the star-forming activity within clumps of these molecular clouds. In this work, we investigate the elongated IRDC G333.73+0.37 (hereafter G333.73), using an assortment of markers to probe the diverse traits of the star-forming activity in the cloud. Based on the results, we hope to be able to comment on the evolutionary stage of the cloud.

G333.73+0.37 is located at a distance of 2.6 kpc (Beltrán et al. 2006; Sánchez-Monge et al. 2013). Previous studies have reported signatures of massive star formation within this IRDC.

Table 1
Details of the Radio Continuum Observations

Frequency (MHz)	610 MHz	1300 MHz
Observation date	2014 Aug 7	2014 Aug 31
On-source time (minutes)	150	164
Bandwidth (MHz)	32	32
Primary beam	45'8	21'8
Synthesized beam	14".5 \times 5".4	5".5 \times 2".0
Position angle (deg)	7.9	5.3
Noise (μ Jy beam ⁻¹)	310	75

Beltrán et al. (2006) mapped the dust emission at 1.2 mm and identified eight massive (14–472 M_{\odot}) cold dust clumps in this region. This IRDC is also associated with an infrared bubble (MWP1G333726+003642) identified by Simpson et al. (2012). High-frequency radio continuum observations at 18 and 22.8 GHz by Sánchez-Monge et al. (2013) identified two sources in this region (beam size $\sim 30''$). These results are chiefly the outcomes of various surveys and hence provide limited information about the IRDC in its entirety. As our motivation is to examine the star-forming potential across the entire IRDC, we use multiwavelength tracers including sensitive radio continuum observations at 1300 and 610 MHz to analyze the morphology and properties of ionized gas associated with newly formed massive stars. In addition, we have utilized the archival infrared and submillimeter data along with the molecular line emission of this region in various molecular species from the MALT90 and ThrUMMS surveys to probe the molecular cloud. Such a plethora of observational data enables a fair visualization of the physical properties, chemistry, kinematics, and evolutionary stage of G333.73.

The organization of the paper is as follows. The details of radio continuum observations and archival data are given in Section 2. Section 3 describes the results of our multi-wavelength study, while Section 4 elaborates on the analysis of the morphology of radio emission, fragmentation, and evolution of cold dust clumps, as well as the kinematics within the IRDC. We also attempt to estimate the age of this filamentary cloud based on objects in different evolutionary stages. Finally, in Section 5, we present our conclusions.

2. Observations and Data Reduction

2.1. Radio Continuum Observations Using Giant Metrewave Radio Telescope

The ionized gas emission from G333.73+0.37 is mapped using the Giant Metrewave Radio Telescope (GMRT) in India (Swarup et al. 1991). GMRT consists of 30 antennas, each having a diameter of 45 m arranged in a Y-shaped configuration. Twelve antennas are distributed randomly in a central array within an area of ~ 1 km², and the remaining 18 antennas are stretched out along three arms, each of length ~ 14 km. The minimum and maximum baselines are 105 m and 25 km, respectively, which allows the simultaneous mapping of small- and large-scale structures. The radio continuum observations were carried out at two frequencies: 1300 and 610 MHz. The angular extent of the largest structure observable with GMRT at 1300 MHz is 7' and 17' at 610 MHz, and our targets have sizes well within these limits. The radio source 3C 286 was used as the primary flux calibrator, while 1626–298 was used

to calibrate the phases. The details of observations are listed in Table 1.

We have carried out data reduction using the NRAO Astronomical Image Processing System (AIPS). The tasks TVFLG and UVFLG were used to remove the visibilities affected by the nonworking antennas and radio frequency interference. The calibrated target data were cleaned and deconvolved using the task IMAGR, and we applied several iterations of self-calibration to minimize the amplitude and phase errors. In addition to creating a map using all the visibilities at 1300 MHz, we have constructed a lower-resolution map at this frequency to examine the low-brightness diffuse emission. This is achieved by limiting the UV range to 25 k λ . A system temperature correction to account for the Galactic plane emission, $(T_{\text{gal}} + T_{\text{sys}})/T_{\text{sys}}$, has been used to scale the fluxes at each frequency, where T_{sys} is the system temperature corresponding to the flux calibrator located away from the Galactic plane. To estimate T_{gal} , we have used the temperature map of Haslam et al. (1982) at 408 MHz. Scaling factors are calculated by extrapolating T_{gal} to 610 and 1300 MHz by assuming a spectral index of -2.6 (Roger et al. 1999; Guzmán et al. 2011), which are then applied to the self-calibrated images. Finally, the flux-scaled maps were corrected for the primary beam using the task PBCOR.

2.2. Archival Data Sets

Apart from radio observations, we have used archival data to investigate emission across the cloud at different wavebands. The properties of the warm dust associated with this region are investigated using mid-infrared *Spitzer Space Telescope* data, and cold dust emission is analyzed using far-infrared and submillimeter maps from *Herschel* Hi-GAL and APEX+*Planck* surveys. In addition, we have used the MALT90 and ThrUMMS spectral line surveys to examine the chemical properties and kinematics of the region.

2.2.1. Spitzer Space Telescope

We have used the mid-infrared maps of this region observed by the *Spitzer Space Telescope*, with a primary mirror of size 85 cm. The Infrared Array Camera (IRAC) is one of the three focal plane instruments that obtain simultaneous broadband images at 3.6, 4.5, 5.8, and 8.0 μ m; the achieved resolutions are 1".7, 1".7, 1".9, and 2".0, respectively (Fazio et al. 2004). We used the Level-2 post-basic calibrated data (PBCD) images from the Galactic Legacy Infrared Mid-Plane Survey (GLIMPSE; Benjamin et al. 2003) to study the nature of diffuse emission. In addition, we have also made use of the MIPS 24 μ m image obtained as a part of the MIPS GAL survey (Carey et al. 2009).

2.2.2. Herschel Hi-Gal Survey

The cold dust emission from the molecular cloud is investigated using images from the *Herschel Space Observatory*. The *Herschel Space Observatory* is a 3.5 m telescope capable of observing in the far-infrared and submillimeter spectral range 55–671 μ m (Pilbratt et al. 2010). The images are part of the *Herschel* Hi-Gal Survey (Molinari et al. 2010). The instruments used in the survey are the Photodetector Array Camera and Spectrometer (PACS; Poglitsch et al. 2010) and the Spectral and Photometric Imaging Receiver (SPIRE; Griffin et al. 2010). The Hi-Gal observations were carried out in

parallel mode covering wavelengths 70–500 μm . We used Level-2.5 PACS images at 70 and 160 μm and Level-3 SPIRE images at 250, 350, and 500 μm for our analysis. The pixel sizes are 2'', 3'', 6'', 10'', and 14'', and the corresponding resolutions are 5'', 13'', 18'', 24'', and 36'' at 70, 160, 250, 350, and 500 μm , respectively. We used the *Herschel* Interactive Processing Environment (HIPE)⁵ to download and process the data.

2.2.3. APEX+Planck Data

The Apex+*Planck* image is a combination of 870 μm data from the ATLASGAL survey (Schuller et al. 2009) and the 850 μm map from the *Planck*/HFI instrument. The data cover emission at larger angular scales, thereby revealing the structure of cold Galactic dust in greater detail (Csengeri et al. 2016). The pixel size and resolution achieved are 3'' and 12'', respectively.

2.2.4. MALT90 Molecular Line Survey

We have used the Millimetre Astronomy Legacy Team 90 GHz Pilot Survey (Foster et al. 2011; Jackson et al. 2013) to understand the properties of the associated molecular gas. This survey has mapped transitions of 16 molecular species near 90 GHz. The observations were carried out using the 8 GHz wide Mopra Spectrometer (MOPS). The data reduction was conducted by the MALT90 team using an automated reduction pipeline. The spatial and spectral resolutions are 72'' and 0.11 km s⁻¹, respectively. The data cubes available from the website are images of size $\sim 4'$. The MALT90 data cube covers only a part of the cloud where there are signatures of active star formation.

2.2.5. ThrUMMS Molecular Line Survey

In order to sample the molecular line emission from the entire IRDC filament, we have used ¹²CO and ¹³CO maps from the Three-mm Ultimate Mopra Milky Way Survey (ThrUMMS; Barnes et al. 2015). The survey mapped the $J = 1 \rightarrow 0$ transition of ¹²CO, ¹³CO, C¹⁸O, and CN lines near 112 GHz at a spectral resolution of 0.1 km s⁻¹ and a spatial resolution of 66''. The data reduction was performed by the ThrUMMS team, and the calibrated data are made available to the public through the website.⁶ In this work, we present only ¹²CO and ¹³CO molecular emission, as C¹⁸O and CN have not been detected owing to relatively poor signal-to-noise ratio.

3. Results

We present our results in the following sequence. As IRDCs have been identified as dark structures against nebulous mid-infrared emission, we initiate our analysis with warm dust emission toward this region. Subsequently, we probe the properties of cold dust and gas in the cloud using far-infrared to millimeter wavelengths. The locations of star-forming flurries are realized using the distribution of ionized gas emission. Finally in this section, we examine the population of YSOs and their distribution across the cloud.

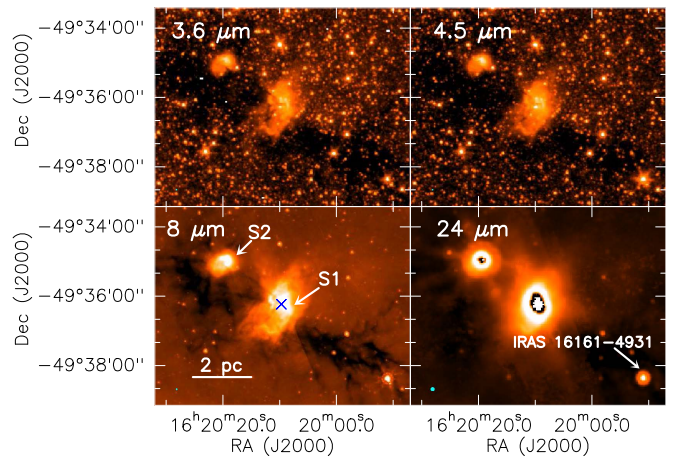


Figure 1. Mid-infrared emission from the IRDC G333.73 at four wavelength bands from *Spitzer*: 3.6, 4.5, 8.0, and 24.0 μm . The dark extinction filaments are clearly seen in the images. We have also marked the locations of two bright infrared sources S1 and S2 in the 8 μm image. The *IRAS* peak corresponding to S1 is indicated with a cross. The position of the *IRAS* source 16161–4931 is marked in the 24 μm image. The corresponding beam sizes (cyan) are shown in the bottom left corner of all panels.

3.1. Mid-infrared Emission from Warm Dust

The mid-infrared maps of the filamentary IRDC G333.73 at 3.6, 4.5, 8.0, and 24 μm bands from *Spitzer* are shown in Figure 1. Two prominent features visually discernible from the maps are the bright infrared objects that we designate S1 and S2. S1 is also cataloged as an infrared bubble (MWP1G333726 +003642; Simpson et al. 2012). These sources appear to be connected by dark filamentary structures silhouetted against nebulous emission. We have not been able to deduce any previously reported information about S2 from our literature survey. We proceed with the assumption that both these regions belong to the same IRDC and that the kinematic distance toward S2 is the same as that of S1, which is 2.6 kpc. The assumption receives support from the molecular line study toward this region, which is discussed in a later section (Section 3.3). In the 24 μm image, S1 and S2 are bright and saturated toward the central regions. S1 is also identified as IRAS 16164–4929, indicated by a cross symbol in the 8 μm map. In addition to S1 and S2, multiple point sources are also observed in the 24 μm map toward the IRDC elongation. A bright 24 μm source, associated with IRAS 16161–4931, is located toward the southwest of the IRDC filament. We discuss this source in more detail in Section 3.7.

The mid-infrared emission is mostly ascribed to small dust grains and could have contributions from (i) thermal emission from warm dust in the circumstellar envelope heated by direct stellar radiation, (ii) heating of dust due to Ly α photons resonantly scattering in the ionized region (Hoare et al. 1991), and (iii) emission due to excitation of polycyclic aromatic hydrocarbons (PAHs) by UV photons in the photodissociation regions (PDRs; Battersby et al. 2011; Nandakumar et al. 2016). The emission in the 4.5 μm band is believed to be dominated by molecular H₂ and CO emission, which traces the shocked molecular gas in active protostellar outflows (Noriega-Crespo et al. 2004; Davis et al. 2007). As the point response functions (PRFs) of 4.5 and 3.6 μm bands are similar, we have constructed a ratio map of [4.5 μm]/[3.6 μm] to study the signatures of outflow within the region. The [4.5]/[3.6] ratio map toward S1 is presented in Figure 2. It has been found that

⁵ HIPE is a joint development by the *Herschel* Science Ground Segment Consortium, consisting of ESA, the NASA *Herschel* Science Center, and the HIFI, PACS, and SPIRE consortia.

⁶ <http://alma-intweb.mtk.nao.ac.jp/~thrumms/>

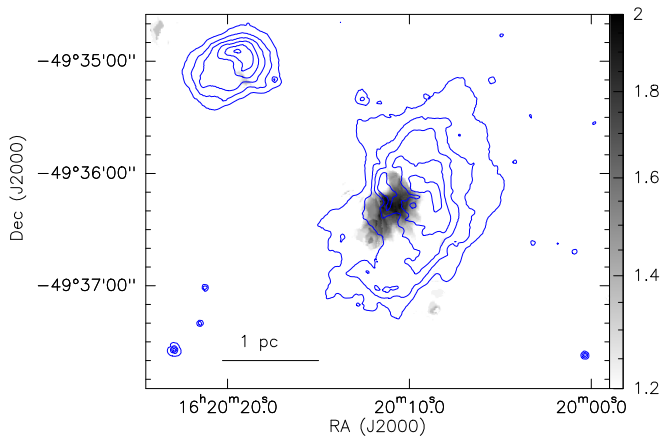


Figure 2. Flux ratio map of *Spitzer* [4.5]/[3.6] overlaid with 8 μ m warm dust contours. The contour levels are 100, 200, 400, 800, 1600, and 3200 MJy Sr⁻¹.

the [4.5]/[3.6] ratio is ~ 1.5 or larger for jets and outflows, whereas it is lower for stellar sources ($\ll 1.5$; Takami et al. 2010; Liu et al. 2013a). In our map, we notice excess [4.5]/[3.6] ratio toward S1, which is located $\sim 20''$ east of the millimeter peak. If the large [4.5]/[3.6] does trace the distribution of shocked gas from the outflow, then it is possible that G333.73 harbors a protostellar outflow (or shocks/winds).

3.2. Properties of Cold Dust Emission

The cold dust emission toward the IRDC is examined using far-infrared and submillimeter maps at seven wavelength bands (70, 160, 250, 350, 500, and 850 μ m and 1.2 mm). The wavelength-dependent variation of emission toward this region is apparent from the *Herschel* and APEX+*Planck* maps (70–850 μ m), presented in Figure 3. The cold dust emission maps exhibit a clumpy structure of the IRDC that spans a region $9'.5 \times 2'.0$, which corresponds to 7.2 pc \times 1.5 pc. The 70 μ m map is morphologically similar to that of the 24 μ m warm dust emission. Unlike the longer-wavelength emission maps, the resemblance of the 70 μ m emission to the warm dust emission at 24 μ m can be attributed to the fact that, apart from the thermal emission due to cold dust, the emission at 70 μ m could also have a contribution from very small dust grains (VSGs; Russeil et al. 2013). The regions S1 and S2 appear to be connected by cold dust filaments as perceived from the longer-wavelength emission maps.

A visual inspection of the 1.2 mm map shows that there are cold dust peaks toward this region in addition to the eight dust clumps identified by Beltrán et al. (2006). We have used the FellWalker algorithm (Berry 2015) to identify clumps in this region. The FellWalker algorithm uncouples peaks based on local gradients, assigning each pixel to the peak that the local gradient points toward. We used a detection threshold of 5σ for identification of peaks, and all the pixels outside the 5σ contour are considered to be noisy. We also set the parameter MinPix as 5, which excluded all clumps with pixels less than 5. Using this algorithm, we detected 10 clumps in G333.73. The peak positions of the clumps are shown in Figure 4. These clumps are labeled as C1, C2,..., C10 in order of their decreasing peak brightness. Overplotted on the image are the apertures corresponding to the area covered by each clump using the FellWalker algorithm.

In order to characterize the individual clumps that can be regarded as sites of local star formation, we have constructed their spectral energy distributions (SEDs). This is achieved by integrating the flux densities within the clump apertures for wavelengths 70 μ m to 1.2 mm. An average sky background, estimated from a nearby field that is $\sim 3'.5$ away (centered at $\alpha_{J2000} = 16^h 19^m 51^s.36$, $\delta_{J2000} = -49^\circ 34' 53''.5$) and devoid of bright diffuse emission, is appropriately subtracted to account for the zero offsets at each wavelength. We fitted the flux densities (F_ν) of the clumps using a modified blackbody function of the form (Gordon 1987; Ward-Thompson & Robson 1990)

$$F_\nu = \Omega B_\nu(T_d)(1 - e^{-\tau_\nu}), \quad (1)$$

where

$$\tau_\nu = \mu m_H \kappa_\nu N(\text{H}_2). \quad (2)$$

Here Ω is the solid angle subtended by the clump, $B_\nu(T_d)$ is the blackbody function at dust temperature T_d , μ is the mean weight of molecular gas taken to be 2.86 assuming that the gas is 70% molecular hydrogen by mass (Ward-Thompson et al. 2010), m_H is the mass of the hydrogen atom, κ_ν is the dust opacity, and $N(\text{H}_2)$ is the molecular hydrogen column density. The dust opacity is estimated using the expression (Ward-Thompson et al. 2010)

$$\kappa_\nu = 0.1 \left(\frac{\nu}{1000 \text{ GHz}} \right)^\beta, \quad (3)$$

where ν is the frequency and β is the dust emissivity index. We have assumed $\beta = 2$ in our analysis (Anderson et al. 2012; Russeil et al. 2013). The best fits were obtained using nonlinear least-squares Marquardt–Levenberg algorithm, considering T_d and $N(\text{H}_2)$ as free parameters. We have assumed a flux density uncertainty of 15% in all bands (Beltrán et al. 2006; Schuller et al. 2009; Launhardt et al. 2013). We find that the fits that include the 70 μ m show larger χ^2_{red} (up to a factor of 3) and larger errors in the parameters (up to 60%) when compared to fits carried out by excluding the 70 μ m flux densities. This is evident from the fits to the SEDs displayed in Figure 5. It is evident that the 70 μ m point exhibits excess emission. Such excess has been observed in other star-forming clouds and has been attributed to the contribution from transiently heated very small grains (e.g., Shetty et al. 2009; Compiègne et al. 2010; Russeil et al. 2013), and its inclusion could overestimate the dust temperature. We proceed with the parameters of fits that exclude the 70 μ m emission, as this characterizes the cold dust in the IRDC. The values of the derived parameters for all the clumps are listed in Table 2. We also note that the ground-based SEST-SIMBA observations failed to pick up large-scale diffuse emission at low flux levels owing to poor sensitivity. Clump 10, being the faintest of all the clumps, has relatively lower flux at 1.2 mm compared to the other bands (Figure 5). We have therefore excluded this 1.2 mm data point from the SED fit in order to get a more robust estimate of parameters for this clump.

The temperature in the clumps lies in the range of 14.3–22.3 K, whereas the column density values lie in the range of $(1.8\text{--}4.9) \times 10^{22} \text{ cm}^{-2}$. Clump C2 exhibits the highest dust

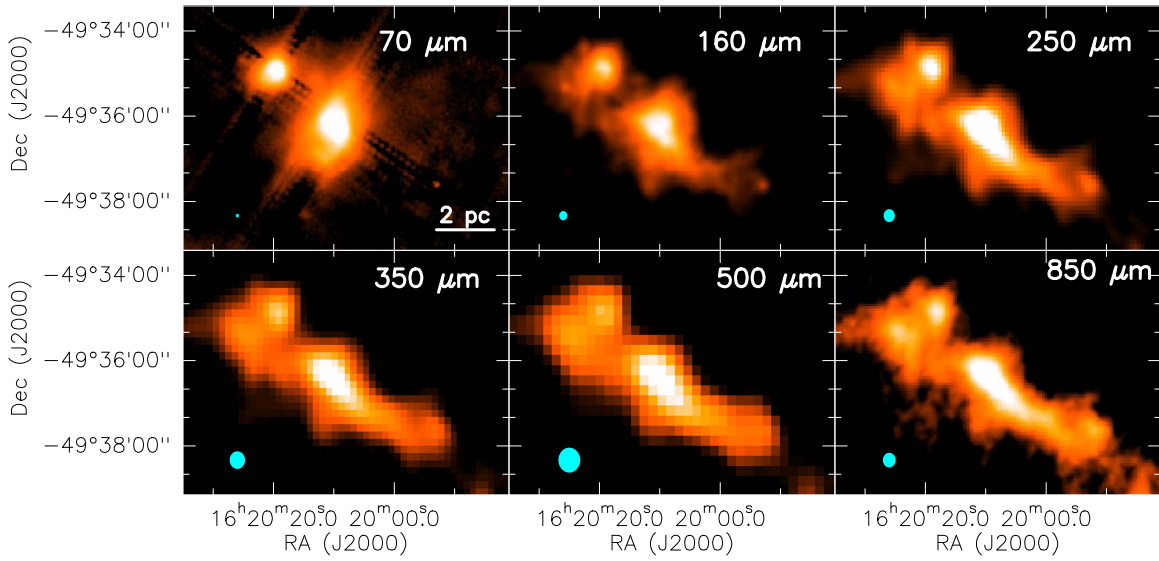


Figure 3. Distribution of cold dust emission toward the G333.73 region at six wavelength bands: 70, 160, 250, 350, and 500 μm from *Herschel* and 850 μm from APEX+*Planck*. The corresponding beam sizes (cyan) are shown toward the bottom left of the individual panels.

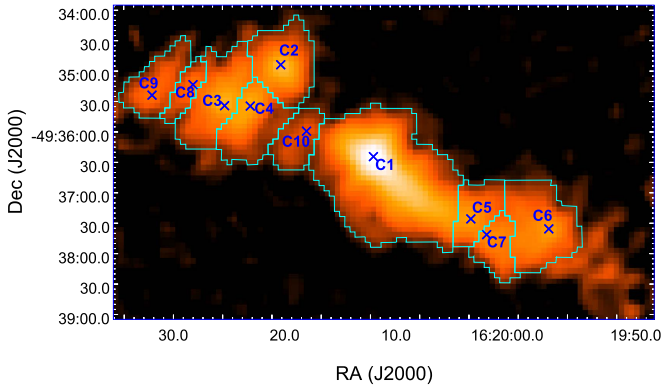


Figure 4. Distribution of cold dust emission toward the G333.73 region at 1.2 mm from SEST-SIMBA. The apertures of 10 mm clumps identified using the FellWalker algorithm are marked in cyan, and the corresponding peak positions are denoted by crosses.

temperature, whereas clump C10 possesses the highest column density. Note that these estimates represent average values over the entire clump. We have also used the column densities of the clumps to estimate their masses (M_c), using the following expression:

$$M_c = N(\text{H}_2) \mu m_{\text{H}} A. \quad (4)$$

Here A represents the physical area of the clump. The clump masses lie in the range 87–1530 M_{\odot} . The total cloud mass is estimated to be $\sim 4700 M_{\odot}$. This is ~ 5 times larger than the 992 M_{\odot} obtained by Beltrán et al. (2006). This difference could be attributed to the following: (i) our estimate of cloud mass is based on the modified blackbody fits using six far-infrared wavelength bands, unlike the latter, which is obtained from only the 1.2 mm map; and (ii) Beltrán et al. (2006) used a value of dust opacity $\kappa_{\nu} \sim 1 \text{ cm}^2 \text{ g}^{-1}$ at 1.2 mm, whereas we have used a different form of the dust opacity law whose value depends on β . Note that $\beta = 2$ leads to $\kappa_{\nu} \sim 0.6 \text{ cm}^2 \text{ g}^{-1}$ at 1.2 mm.

We have also estimated the surface density (Σ) of the individual clumps, defined as M_c/A , a parameter that can be used to probe massive star formation in the clumps. According to Krumholz & McKee (2008), clouds with a minimum surface density of $\Sigma \sim 1 \text{ g cm}^{-2}$ would be able to form massive stars by suppressing fragmentation. The surface density values for clumps in G333.73 are listed in Table 2. The values of Σ for the 10 clumps lie in the range 0.1–0.3 g cm^{-2} . The maximum Σ is observed toward clump C10, which also displays the largest column density among clumps. Observational studies toward a large sample of massive star-forming cores, such as those by López-Sepulcre et al. (2010), Miettinen & Harju (2010), and Giannetti et al. (2013), have shown that massive star-forming cores possess lower surface densities of the order of $\sim 0.2 \text{ g cm}^{-2}$. According to the latter gauge, six of our clumps have the potential to form massive stars. This is substantiated by our assertion that the surface density value of a clump represents a sort of average, and the actual surface density could be higher near the peak emission or dense core considering that the sizes of the clumps are large ($>0.6 \text{ pc}$).

3.2.1. Maps of Column Density and Dust Temperature

In addition to the clump SEDs, we have constructed the line-of-sight-averaged molecular hydrogen column density and dust temperature maps of this region with the intention of understanding the small-scale variations across the IRDC, in addition to comparing this with molecular line emission maps. The maps are created by carrying out a pixel-to-pixel graybody fit in the selected wavelength regime (160 μm –1.2 mm) using the equations discussed earlier. If we consider all the wavelengths, the resolution of the map is limited by emission at the wavelength that has the lowest resolution, i.e., $36''/4$ at 500 μm . Since the longer-wavelength data are well sampled, we prefer to construct higher-resolution maps. To achieve this, we excluded the 500 μm image from the analysis. The remaining maps at 160, 250, 350, and 850 μm and 1.2 mm are convolved and regridded to the resolution ($25''$) and pixel size ($10''$) of the 350 μm image. As the sensitivity of the 1.2 mm map is lower, we are unable to sample the diffuse emission extending beyond

Table 2
Molecular Clumps Identified in This Region

Clump	α_{J2000} (h m s)	δ_{J2000} ($^{\circ}$ ' ")	Area (pc ²)	Temperature (K)	Column density (10 ²² cm ⁻²)	χ^2_{red}	Mass (M_{\odot})	Σ (g cm ⁻²)
C1	16:20:09.693	-49:36:24.99	2.3	20.8 \pm 1.7	2.8 \pm 0.6	2.4	1530	0.1
C2	16:20:19.091	-49:34:53.54	0.6	22.3 \pm 1.9	1.9 \pm 0.6	4.0	266	0.1
C3	16:20:24.837	-49:35:34.14	0.6	16.1 \pm 3.2	3.2 \pm 0.9	4.8	456	0.2
C4	16:20:22.226	-49:35:34.16	0.6	16.4 \pm 1.4	2.9 \pm 0.9	5.8	420	0.2
C5	16:20:00.287	-49:37:25.91	0.4	15.1 \pm 1.1	3.7 \pm 0.9	4.2	350	0.2
C6	16:19:51.925	-49:37:36.01	0.7	14.3 \pm 1.2	3.7 \pm 0.1	7.2	612	0.2
C7	16:19:58.196	-49:37:41.13	0.3	15.6 \pm 1.4	2.5 \pm 0.8	6.1	180	0.1
C8	16:20:27.990	-49:35:13.52	0.2	15.9 \pm 1.5	1.8 \pm 0.6	7.1	87	0.1
C9	16:20:32.144	-49:35:23.76	0.5	16.4 \pm 1.4	3.8 \pm 1.1	5.4	451	0.2
C10	16:20:16.481	-49:35:59.42	0.3	15.1 \pm 0.7	4.9 \pm 0.9	1.5	353	0.3

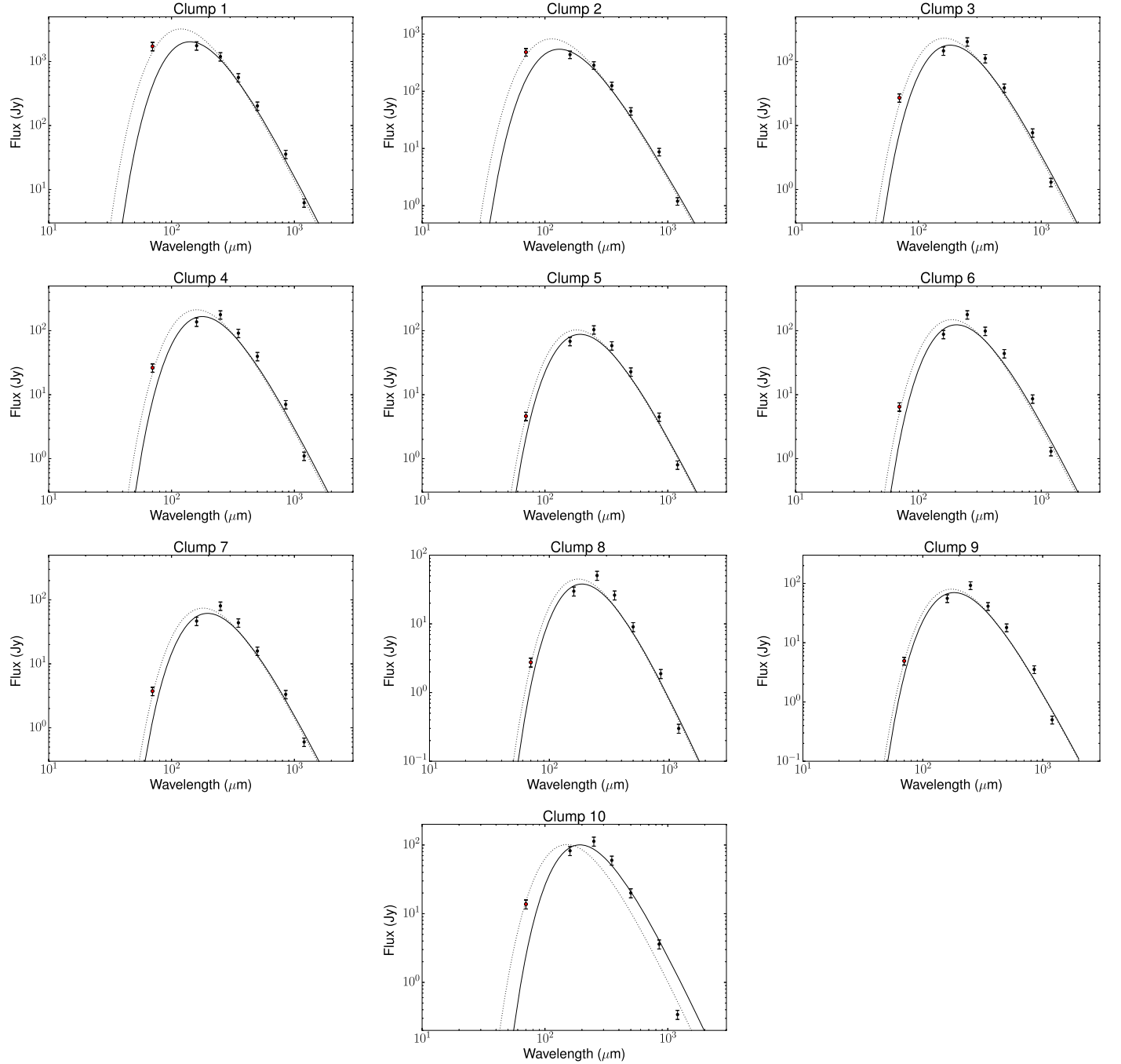


Figure 5. SEDs of the cold dust clumps in G333.73. Flux densities from 160 μm to 1.2 mm are represented as filled circles, and the 70 μm flux is represented as a red dot. The best-fit modified blackbody function for each SED excluding 70 μm is shown as a solid line, and the fit including 70 μm flux is shown as a dotted line. The error bars correspond to 15% uncertainties in flux densities.

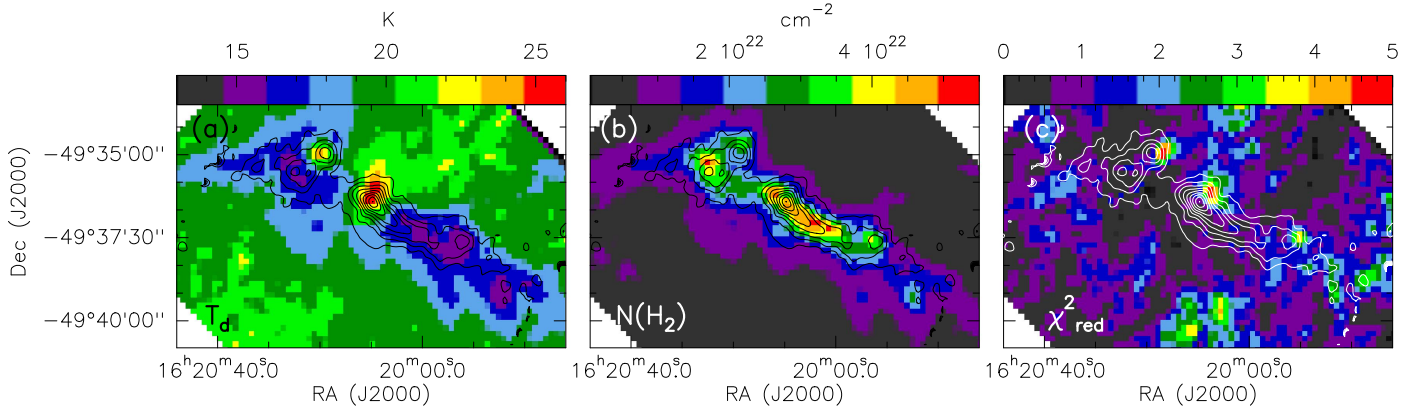


Figure 6. (a) Dust temperature (T_d), (b) column density ($N(\text{H}_2)$), and (c) reduced chi-square (χ^2_{red}) maps of the G333.73 region obtained from the modified blackbody fit toward individual pixels overlaid with 1.2 mm cold dust contours. The contour levels are from 75 to 1200 mJy beam $^{-1}$ in steps of 100 mJy beam $^{-1}$.

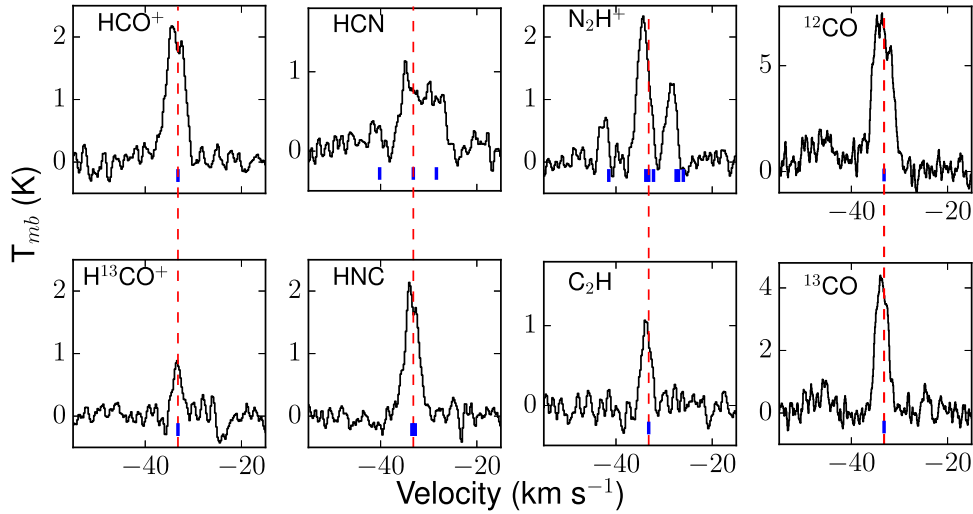


Figure 7. Spectra of eight molecular lines toward the HCO^+ peak position smoothed to a velocity smoothing of 0.4 km s^{-1} . The LSR velocity of the cloud is estimated from the H^{13}CO^+ line as -33.2 km s^{-1} , indicated by a red dashed line in all six panels. The hyperfine components of each species are marked as blue lines in the individual panels. The velocities of hyperfine components are estimated assuming an LSR velocity of -33.2 km s^{-1} .

the high-density regions. For these pixels, the values of χ^2_{red} are larger. To obtain better fits, the pixels with $\chi^2_{\text{red}} > 2$ owing to noisy 1.2 mm emission were fitted anew by excluding the 1.2 mm data point from the SED fit.

The dust temperature, column density, and reduced chi-square (χ^2_{red}) maps are presented in Figure 6. For further analysis, we have considered pixels within the 5σ contour of the 1.2 mm map. The peak column density is $5.5 \times 10^{22} \text{ cm}^{-2}$, whereas the mean column density is $2.4 \times 10^{22} \text{ cm}^{-2}$. The column density distribution is clumpy in nature, exhibiting multiple peaks. The temperature within the IRDC ranges from 14.8 to 25.4 K with a mean value of 18 K. The temperature map is peaked toward the location of S1. The temperature map also reveals an additional peak that matches with the location of S2. These temperature peaks can be understood based on the morphology of $160 \mu\text{m}$ emission. The $160 \mu\text{m}$ emission is the shortest wavelength used in the SED construction and traces the warmest dust emission components. Hence, pixels with significant emission at $160 \mu\text{m}$ are weighted by the corresponding flux density, leading to a higher dust temperature

that signifies higher levels of star formation activity here. The low values of dust temperature are observed toward the dark filaments in the $8 \mu\text{m}$ map.

3.3. Molecular Line Emission from G333.73

The kinematics and chemistry of IRDCs can be investigated using molecular line emission. For the IRDC G333.73, we use molecular line data from the MALT90 pilot survey that covers a region of size $\sim 4'$ centered on S1 in clump C1. Six molecular species have been detected toward this region: HCO^+ , H^{13}CO^+ , HCN, HNC, N_2H^+ , and C_2H . The spectra of these molecules at the location of the emission peak of HCO^+ are shown in Figure 7. The LSR velocity of the region (hence IRDC) is estimated using a single transition of H^{13}CO^+ assuming the line to be optically thin. We have fitted a single Gaussian profile to the spectrum and determined the LSR velocity as -33.2 km s^{-1} . This is consistent with the LSR velocity of -33.0 km s^{-1} estimated from the CS (2–1) line (Bronfman et al. 1996). The hyperfine components of HCN and N_2H^+ molecules are clearly discerned in the velocity profiles.

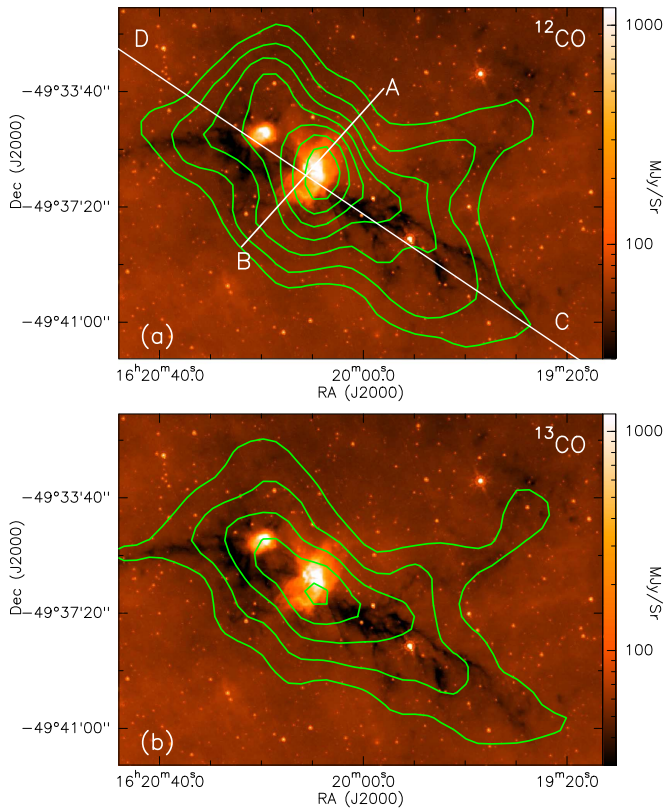


Figure 8. *Spitzer* 8 μm map overlaid with (a) ^{12}CO and (b) ^{13}CO contours. Contour levels are 13–35 K km s^{-1} in steps of 3.1 K km s^{-1} for panel (a) and 4.5–15 K km s^{-1} in steps of 2.1 K km s^{-1} for panel (b). Lines AB and CD are the lines along which PV diagrams are constructed.

HCN has three hyperfine components that are well separated ($+5$ and -7 km s^{-1} , respectively). N_2H^+ has seven hyperfine components. The profiles of HCO^+ and HNC lines exhibit a blue asymmetric feature characterized by self-absorption dips in the lines, with relatively strong blue peaks with respect to red peaks. We explore the likely origin of the asymmetric profile in the next section.

As the MALT90 survey has limited coverage, we are unable to sample the molecular gas kinematics of the entire IRDC filament. We therefore utilize the ^{12}CO and ^{13}CO data from the ThrUMMS survey for this purpose. The CO spectra toward the peak position of HCO^+ emission are shown in Figure 7 (last column). These spectra exhibit blue asymmetric profiles similar to those of HCO^+ and HNC . The distribution of CO emission with respect to warm dust emission is shown in Figure 8. From the maps, it is evident that the CO emission extends well beyond the apparently dark filamentary structure. This is in accordance with expectations, as the ^{12}CO and ^{13}CO lines also sample the diffuse envelope, being low-density tracers.

3.3.1. Blue Asymmetry of HCO^+ and HNC Profiles

The HCO^+ line is optically thick based on the expected ratio of line intensities of HCO^+ and H^{13}CO^+ . Similarly, we proceed with the supposition that HNC is optically thick. Although both display a double-peaked structure, HCO^+ is a single transition line, whereas HNC has three hyperfine components within 0.5 km s^{-1} , marked in Figure 7. These lines are considered good infall and outflow tracers. An examination of the HCO^+ and HNC velocity profiles shows

Table 3
Best-fit Parameters for the Two-layer Infall Model

Parameter	Component 1	Component 2
Column density (10^{14} cm^{-2})	16.1 ± 2.7	0.2 ± 0.03
T_{ex} (K)	31.1 ± 0.5	7.1 ± 0.5
FWHM (km s^{-1})	1.9 ± 0.1	2.8 ± 0.2
Size (arcsec)	23.7 ± 1.4	31.1 ± 4.1
V_{LSR} (km s^{-1})	-33.4 ± 0.1	-33.0 ± 0.1

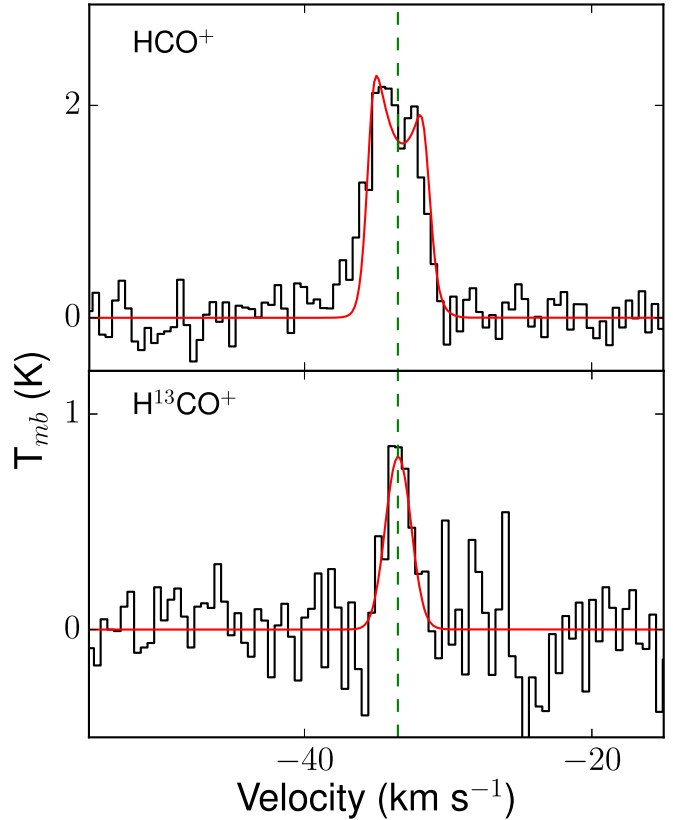


Figure 9. Spectrum toward the peak of HCO^+ and H^{13}CO^+ emission. The red line represents the best-fit model using the two-layer infall process for the optically thick HCO^+ line and its optically thin isotopologue H^{13}CO^+ line. The dashed line (green) indicates the LSR velocity of -33.2 km s^{-1} .

that they exhibit significant blue asymmetry in their profiles indicative of infall in this region (Miettinen 2012; Jin et al. 2016). Blue asymmetry could also arise from rotation and outflow (e.g., Redman et al. 2004). The velocity of the absorption dip agrees well with that of the LSR velocity estimated from the H^{13}CO^+ line. The velocities of the blueshifted peaks of the HCO^+ and HNC lines relative to the LSR velocity are -0.9 and -0.8 km s^{-1} , respectively. Similarly, the velocities of the redshifted peaks with respect to the LSR velocity are 1.0 and 0.8 km s^{-1} , respectively. These values indicate that the red and blue peaks are quite symmetric with respect to the LSR velocity. We next scrutinize the intensities, and to quantify the blue-skewed profile, we have used the asymmetry parameter δV . This is defined as the difference between the peak velocities of the optically thick line, V_{thick} (of HCO^+/HNC in our case), and the optically thin line, V_{thin} (of H^{13}CO^+), divided by the FWHM of the optically

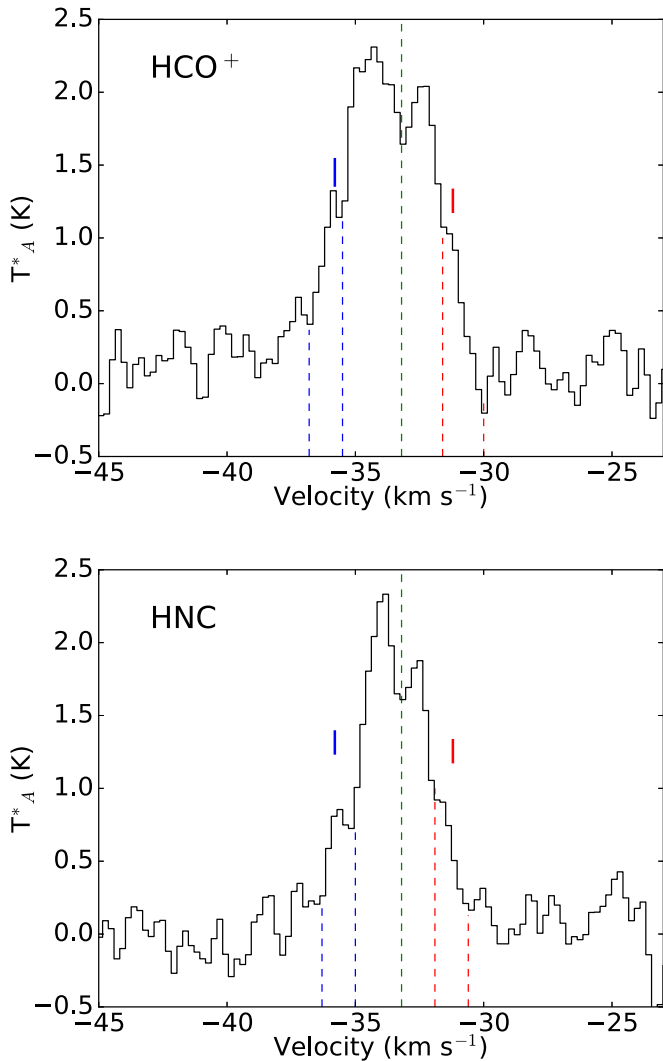


Figure 10. Spectrum of HCO^+ and HNC molecules toward peak emission. The location of the blue and red wings seen toward both the spectra is indicated with solid lines.

thin line represented as ΔV (Yu & Wang 2013):

$$\delta V = \frac{V_{\text{thick}} - V_{\text{thin}}}{\Delta V_{\text{thin}}}.$$

Using a V_{thin} of -33.2 km s^{-1} and ΔV_{thin} of 2.2 km s^{-1} from the Gaussian fit to the H^{13}CO^+ profile, we obtain a δV of -0.4 for both the lines. This is characterized as a blue profile according to the criterion of Mardones et al. (1997), who use $\delta V < -0.25$ to designate a profile as blue.

3.3.2. HCO^+ Line Profile Analysis Using LTE Modeling

To study the likely mechanisms responsible for the observed blue asymmetry in the HCO^+ line, we carried out a two-component LTE modeling in CASSIS software (Caux et al. 2011). For the modeling, we considered the HCO^+ line and its isotopologue, H^{13}CO^+ . The observed self-absorbed profile of the HCO^+ line can be explained if we use a two-layer model where there is a warm emitting component and a cold absorbing component. For a better signal-to-noise ratio, we have integrated the emission within $20''$ of the HCO^+ peak for both HCO^+ and H^{13}CO^+ lines. The best fit to the profiles is

obtained by varying the parameters such as line width, V_{LSR} , excitation temperature, column density, and source size. The $[\text{HCO}^+]/[\text{H}^{13}\text{CO}^+]$ abundance ratio is assumed to be 50 (Purcell et al. 2006). The fitted spectrum is shown in Figure 9, and the results of the radiative analysis are presented in Table 3. The characteristics of the two components are as follows: a warm component with an excitation temperature of 31.1 K and column density of $1.6 \times 10^{15} \text{ cm}^{-2}$, and a cold, absorbing component with lower excitation temperature (7.1 K) and column density ($2.0 \times 10^{13} \text{ cm}^{-2}$). The velocity of the cold component is redshifted by 0.4 km s^{-1} with respect to the warm component. This could be construed as cold molecular gas in the outer envelope receding toward the inner warmer regions and interpreted as protostellar infall. The overall blue asymmetric profile fits well using LTE modeling, although we see some additional red and blue components that cannot be explained through the infall scenario alone (see Figure 10). These additional peaks require multiple components, suggesting the presence of small-scale outflows in the region. Observations with better spatial resolution and sensitivity are essential to enhance our understanding of the profiles.

3.3.3. Mass Infall Rate

Considering that the blue asymmetry of HCO^+ and HNC lines suggests protostellar infall, the mass infall rate (\dot{M}_{inf}) of the circumstellar envelope can be estimated using the expression $\dot{M}_{\text{inf}} = 4\pi R^2 V_{\text{inf}} \rho$ (López-Sepulcre et al. 2010), where $V_{\text{inf}} = V_{\text{thin}} - V_{\text{thick}} = V_{\text{H}^{13}\text{CO}^+} - V_{\text{HCO}^+}$ is an estimate of the infall velocity, $\rho = M/(4/3\pi R^3)$ is the average clump volume density, and R is the radius of the clump, calculated using the dust continuum emission. We estimate V_{inf} as 0.9 km s^{-1} and $M \sim 1530 M_{\odot}$ and $R \sim 0.9 \text{ pc}$ for clump C1, and we obtain an \dot{M}_{inf} of $4.7 \times 10^{-3} M_{\odot} \text{ yr}^{-1}$. This is in congruence with that estimated toward other infall candidates. For example, López-Sepulcre et al. (2010) obtained infall rates ranging from 10^{-3} to $10^{-1} M_{\odot} \text{ yr}^{-1}$ for a sample of high-mass star-forming clumps. He et al. (2015) inferred median mass infall rates of $(7-8) \times 10^{-3} M_{\odot} \text{ yr}^{-1}$ for prestellar, protostellar, and ultracompact H II region stages from their sample of massive star-forming regions. They concluded that the infall rate is independent of the evolutionary stage.

3.3.4. Velocity Structure of the Cloud

The position–velocity (PV) diagram serves as a useful tool to understand the large-scale kinematics of a region. The PV diagrams of ^{12}CO and ^{13}CO are constructed along two directions: (i) AB, perpendicular to the long axis of the cloud (P.A. = $47^\circ 3$), and (ii) CD, which is parallel to the IRDC long axis (P.A. = $134^\circ 2$). These directions are shown in Figure 8(a). The PV plots are presented in Figure 11. The zero offset in the PV diagrams corresponds to the position $\alpha_{\text{J2000}} = 16^{\text{h}}20^{\text{m}}10^{\text{s}}.7$ and $\delta_{\text{J2000}} = -49^\circ 36' 18''.8$. Along AB toward the center position, the blue and red components are clearly visible in both species, with the blue component brighter than the red, suggesting infall. Along CD, we observe a velocity gradient from C to D (i.e., southwest to northeast). The overall velocity gradient is approximately 5 km s^{-1} in magnitude, spanning a region of $10'$ from west to east, i.e., $0.7 \text{ km s}^{-1} \text{ pc}^{-1}$. We also detect few additional substructures in velocity, evident from the ^{13}CO velocity map shown in Figure 12. Velocity gradients of this nature have been observed in other star-forming regions.

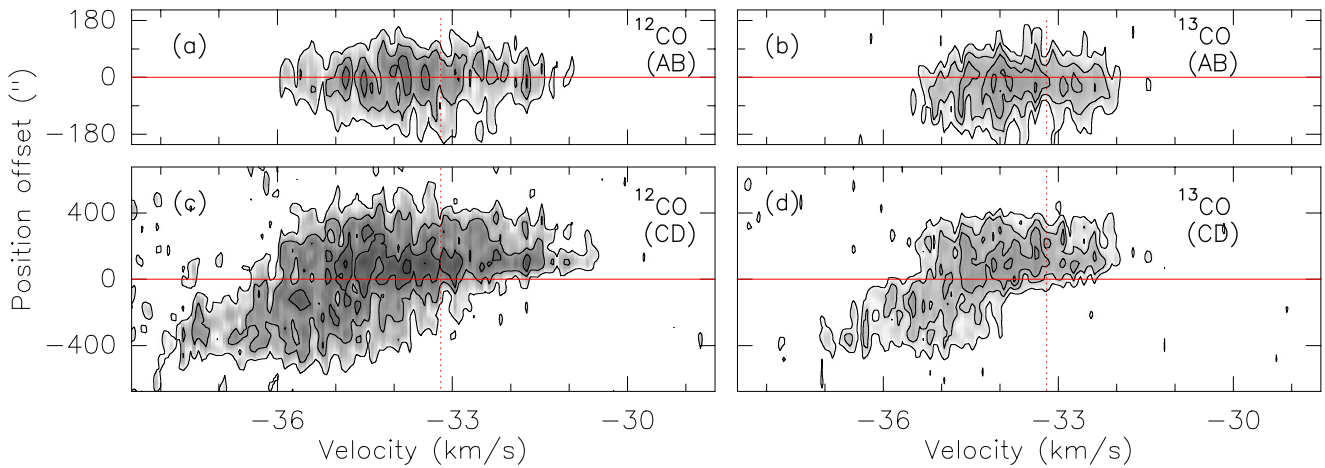


Figure 11. Position–velocity diagrams of ^{12}CO and ^{13}CO molecules. Panels (a) and (b) are along the cut AB shown in Figure 8(a), and panels (c) and (d) are along the CD shown in Figure 8(a). The solid line marks the location of zero offset, and the dashed line denotes the LSR velocity.

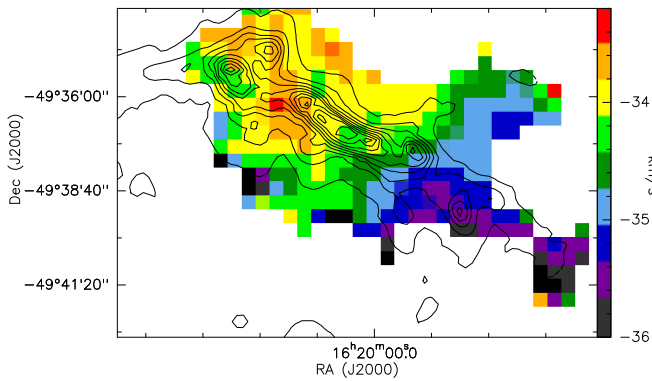


Figure 12. Velocity (first-moment) map of the ^{13}CO line overlaid with column density contours. The contour levels are from $1 \times 10^{22} \text{ cm}^{-2}$ to $6 \times 10^{22} \text{ cm}^{-2}$ in steps of $7.3 \times 10^{21} \text{ cm}^{-2}$.

For example, Sokolov et al. (2017) find a velocity gradient of $0.2 \text{ km s}^{-1} \text{ pc}^{-1}$ in the IRDC filament G035.39-00.33 of length 6 pc. From their study toward a sample of 54 filaments in the northern Galactic plane, Wang et al. (2016) estimate a mean velocity gradient of $0.4 \text{ km s}^{-1} \text{ pc}^{-1}$ toward the filaments. The systematic velocity gradient observed in the IRDC studied here could hint at the rotation and/or accretion flows along the cloud. This is explored in detail in Section 4.4.

3.4. Intensity Distribution of Molecular Gas

In this section, we examine the morphology of the molecular line emission associated with the IRDC. The distribution of CO is apparent from Figure 8, while Figure 13 shows the integrated intensity (zeroth-moment) maps of the six molecular species from the MALT90 survey. The peak of the molecular line emission appears shifted toward the south of the column density peak (estimated from dust continuum emission) by $\sim 15''$ (within clump C1). This could be attributed to resolution effects, as the beam size of the molecular gas emission is nearly three times larger than that of dust continuum emission. Besides, the role of optical depth effects cannot be ruled out. The detailed properties of individual species are discussed below.

3.4.1. ^{12}CO and ^{13}CO (Carbon Monoxide)

CO is the most easily observed molecular line in the interstellar medium and is present even in fairly tenuous gas (Dame et al. 2001). Generally, the ^{12}CO line is optically thick and, with ^{13}CO being relatively optically thin, can trace higher-density gas ($n_{\text{H}_2} > 10^3 \text{ cm}^{-3}$) in molecular clouds. In the present case, ^{13}CO is also optically thick as evident from Figure 7. The distribution of ^{12}CO and ^{13}CO emission in G333.73 is shown in Figure 8 and displays elongated morphology consistent with cold dust emission and column density maps. The aspect ratio of ^{13}CO (~ 5) is more than twice that of ^{12}CO (~ 2). Moreover, the ^{12}CO emission toward S2 is extended compared to ^{13}CO . This could be due to the fact that ^{12}CO is a low-density gas tracer compared to the latter and hence traces the extended envelope surrounding the dense gas. We also see an extension toward the northwest in both of the CO maps that overlaps with an extinction filament in the warm dust emission.

3.4.2. HCO^+ and H^{13}CO^+ (Formylium)

The HCO^+ ion has been used to investigate the infall and outfall motions (e.g., Codella et al. 2001; Fuller et al. 2005; Cyganowski et al. 2011); hence, the $\text{HCO}^+ J = 1-0$ is believed to be a good tracer of kinematics in star-forming regions (e.g., Sun & Gao 2009; Rygl et al. 2013). However, this transition could be optically thick as a result of contributions from various mechanisms and gas motions within the clumps. Consequently, higher transitions of HCN, HNC, and HCO^+ have been suggested as more favorable infall tracers (Chira et al. 2014).

HCO^+ is detected close to the peak of the cold dust emission, and the distribution is nearly spherical (see Figure 13). Weak HCO^+ emission is detected toward the other millimeter peaks of the IRDC (C2, C7) within the sampled region. H^{13}CO^+ is a high-density tracer and is generally assumed to be optically thin. The distribution of H^{13}CO^+ is morphologically different as compared to the HCO^+ emission, and we discern that the intensity is relatively weak toward the peak location of other molecular species such as HCO^+ . This is a region where most of the ionized gas emission is distributed. The lower intensity of H^{13}CO^+ emission toward S1 could be attributed to the destruction of this species by UV radiation and

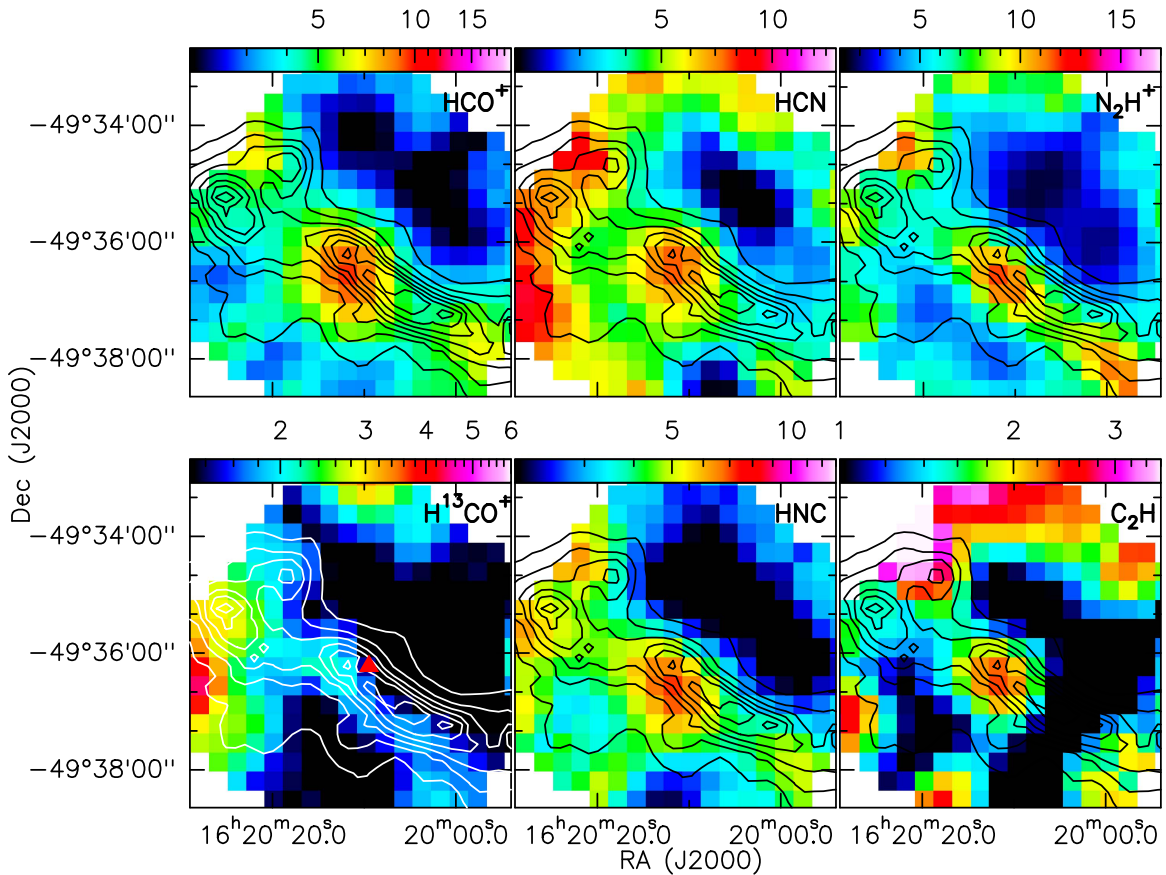


Figure 13. Integrated intensity maps of six molecular lines (labeled in the top right corners) detected toward G333.73 overlaid with column density contours. The contour levels are from $1 \times 10^{22} \text{ cm}^{-2}$ to $6 \times 10^{22} \text{ cm}^{-2}$ in steps of $7.3 \times 10^{21} \text{ cm}^{-2}$. We show the integrated intensity maps of HCO^+ ($V = [-38.5, -29.5] \text{ km s}^{-1}$), H^{13}CO^+ ($V = [-35.5, -30.7] \text{ km s}^{-1}$), HCN ($V = [-37.7, -23.9] \text{ km s}^{-1}$), HNC ($V = [-38.5, -29.0] \text{ km s}^{-1}$), N_2H^+ ($V = [-44.5, -25.2] \text{ km s}^{-1}$), and C_2H ($V = [-36.3, -31.5] \text{ km s}^{-1}$). The color intensity scale is in units of K km s^{-1} . The triangle in the bottom left panel (H^{13}CO^+) corresponds to the IRAS peak position.

high-density electrons, as the abundance of H^{13}CO^+ is a factor of 50 lower than that of HCO^+ (e.g., Goicoechea et al. 2009; Veena et al. 2017).

3.4.3. HCN (Hydrogen Cyanide) and HNC (Hydrogen Isocyanide)

The HCN molecule and its metastable geometrical isomer HNC are typically employed as dense gas tracers in analyzing the chemistry of star-forming regions (e.g., Liu et al. 2013b; Miettinen 2014). In particular, the HNC molecule is considered a good tracer of infall motion (Kirk et al. 2013). In the IRDC G333.73, we detect both HCN and HNC molecules with optically thick profiles. The morphologies of HCN and HNC emission are similar to that of HCO^+ emission. The hyperfine components of HCN are visible in the spectrum but display heavy self-absorption. HNC exhibits a strong blue asymmetry similar to the HCO^+ line. Similar to the HCO^+ integrated intensity map, additional peaks (associated with clumps) are also seen toward the northeast and southwest directions.

3.4.4. N_2H^+ (Diazenylium) and C_2H (Ethyne)

The N_2H^+ ion is regarded as a good tracer of dense gas, as it resists freeze-out on dust grains compared to the carbon-bearing species (Bergin & Langer 1997; Charnley 1997). Thus, it is favored in the studies of cold molecular clumps and cores where other species such as CO and CS are depleted. The distribution of N_2H^+ emission in G333.73 is similar to the

HCO^+ , HCN , and HNC molecules, but the shape of the clump is elongated (similar to continuum emission from dust), unlike the other species, which show a spherical distribution.

The species C_2H is believed to form through photodissociation of the acetylene molecule and is acknowledged as a good tracer of PDRs (Ginard et al. 2012). A recent study by Beuther et al. (2008) has shown that C_2H is observed in all stages of high mass evolution from IRDCs to massive protostellar objects to ultracompact H II regions. The distribution of C_2H is spherical in morphology and similar to other molecules such as HCO^+ , HCN , and HNC toward the peak emission region. However, unlike the other species, the emission is not extended in the direction of the filament, but appears rather confined to clump C1. The lack of C_2H emission toward the immediate southwest of peak emission, where the extinction is high, is noticeable. Evidence of secondary peaks is observed toward S2 and toward the southwest of the IRDC. As the location of peak emission matches with that of other high-density tracers, we infer that the C_2H emission close to the continuum peak is possibly originating from the molecular cloud itself rather than from the PDR.

3.5. Ionized Gas Emission

The radio continuum emission from G333.73+0.37 at 1300 and 610 MHz is shown in Figure 14. The ionized gas emission at 1300 MHz toward S1 reveals a shell-like structure surrounded by a low surface brightness diffuse envelope as

Table 4
Properties of Sources S1 and S2 from Radio Continuum Data

Source	Diameter (pc)	EM (pc cm ⁻⁶)	n_e (cm ⁻³)	N_{Lyc} (10 ⁴⁶ s ⁻¹)	Spectral Type	R_s (pc)	t_{dyn} (Myr)
S1	0.38	2.4×10^5	734	22.9	O9.5-B0	0.03	0.2
S2	0.15	2.9×10^5	1313	4.2	B0-B0.5	0.02	0.01

seen in Figure 14(a). The shell structure is more evident in the high-resolution map, displayed in Figure 14(b), with two peaks separated by lower flux density toward the center, giving the appearance of a cleft ring. The angular diameter of the shell structure is $\sim 30''$, which corresponds to 0.4 pc at a distance of 2.6 kpc. The radio emission at 610 MHz shown in Figure 14(c) shows a more compact structure, and traces of the shell are not evident. While resolution effects could play a role, the data quality is poor compared to the higher-frequency image, as the diffuse structure is not visible either. There exists, however, a possibility that optical depth effects could hamper our viewing of the shell structure. We also detect radio emission toward source S2, where the emission is highly compact. This suggests that S2 is relatively young and/or excited by a lower-mass zero-age main-sequence (ZAMS) star. Additionally, two point-like sources, designated P1 and P2, are detected toward the southwest and southeast of S1, marked in Figure 14(a). These are not positionally coincident with any infrared emission/source.

We have computed the spectral indices ($\alpha_{610-1300}$) of the compact sources by integrating flux densities at 610 and 1300 MHz. For S2, we estimate the spectral index as -0.28 . For P1 and P2, we obtain steeper spectral indices of -2.0 and -0.4 , respectively. These values are indicative of a nonthermal contribution to the radio emission (Kobulnicky & Johnson 1999), as thermal emission from H II regions typically falls in the range $-0.1 \leq \alpha \leq 2$ (Olson 1975). The latter two are likely to be background sources of extragalactic origin, and we exclude them from further analysis in this work.

We estimate the radio properties of both the H II regions, S1 and S2, to learn about the source(s) of excitation, as well as the physical conditions such as ionized gas densities within these regions. The emission measure (EM), electron density (n_e), and Lyman continuum photon rate (N_{Lyc}) under the assumptions of optically thin emission and negligible absorption by dust are given by the following relations (Schmiedeke et al. 2016):

$$\left(\frac{\text{EM}}{\text{pc cm}^{-6}} \right) = 3.217 \times 10^7 \left(\frac{S_\nu}{\text{Jy}} \right) \left(\frac{T_e}{\text{K}} \right)^{0.35} \times \left(\frac{\nu}{\text{GHz}} \right)^{0.1} \left(\frac{\theta_{\text{src}}}{\text{arcsec}} \right)^{-2}, \quad (5)$$

$$\left(\frac{n_e}{\text{cm}^{-3}} \right) = 2.576 \times 10^6 \left(\frac{S_\nu}{\text{Jy}} \right)^{0.5} \left(\frac{T_e}{\text{K}} \right)^{0.175} \times \left(\frac{\nu}{\text{GHz}} \right)^{0.05} \left(\frac{\theta_{\text{src}}}{\text{arcsec}} \right)^{-1.5} \left(\frac{d}{\text{pc}} \right)^{-0.5}, \quad (6)$$

$$\left(\frac{N_{\text{Lyc}}}{\text{s}^{-1}} \right) = 4.771 \times 10^{42} \left(\frac{S_\nu}{\text{Jy}} \right) \left(\frac{T_e}{\text{K}} \right)^{-0.45} \left(\frac{\nu}{\text{GHz}} \right)^{0.1} \left(\frac{d}{\text{pc}} \right)^2, \quad (7)$$

where S_ν is the flux density at frequency ν , T_e is the electron temperature, θ_{src} is the angular source size, and d is the distance

to the source. In order to estimate the electron temperature in this region, we apply the electron temperature gradient curve across the Galactic disk (Churchwell et al. 1978; Quireza et al. 2006) and obtain a value of 6800 K for a galactocentric distance of 6.3 kpc. To determine the properties of S2, we use the same kinematic distance of 2.6 kpc as S1, since the LSR velocity of molecular gas close to S2 is similar to what we measured toward S1. The radio properties of S1 and S2 determined from the above equations are listed in Table 4. Assuming that the H II regions are excited by a single ZAMS star, S1 is ionized by a late O or early B type star, while S2 is powered by an early B star. The electron density toward S2 is nearly a factor of two larger than that toward S1. Equipped with the knowledge of the Lyman continuum flux and electron density, we estimate the radius of the Strömgren sphere, defined as the radius at which the rate of ionization equals that of recombination under the assumption that the H II region is expanding in a homogeneous and spherically symmetric medium. The radius of the Strömgren sphere, R_s , is given by the expression

$$R_s = \left(\frac{3 N_{\text{Lyc}}}{4 \pi n_0^2 \alpha_B} \right)^{1/3}. \quad (8)$$

Here α_B is the radiative recombination coefficient assumed to be $2.6 \times 10^{-13} \text{ cm}^3 \text{ s}^{-1}$ (Osterbrock 1989); n_0 represents the mean number density of atomic hydrogen, which is estimated from the column density map using the expression $n_0 = 3N(\text{H}_2)/2R$, where R is the radius of the clump. Here n_0 is $1.6 \times 10^4 \text{ cm}^{-3}$ and $2.3 \times 10^4 \text{ cm}^{-3}$ for clumps C1 and C2, corresponding to S1 and S2, respectively. From the above expression, we found R_s to be 0.03 and 0.02 pc for S1 and S2, respectively. If we compare this with the observed radii of S1 and S2, we find that the observed radii are an order of magnitude higher compared to the R_s values determined. This signifies that the H II regions have expanded beyond the Strömgren spheres and are in the second expansion phase, where pressure disturbances from within the H II region are able to cross the ionization front and create an expanding shock. We can estimate the dynamical age, t_{dyn} , of these H II regions based on a simple model of an expanding photoionized nebula, in a homogeneous medium using the size of radio emission (Dyson & Williams 1980). The expression for t_{dyn} is given by

$$t_{\text{dyn}} = \left(\frac{4 R_s}{7 c_i} \right) \left[\left(\frac{R}{R_s} \right)^{7/4} - 1 \right], \quad (9)$$

where R represents the radius of the spherical H II region and c_i is the isothermal sound speed in the ionized gas, assumed to be

Table 5
Coordinates and Magnitudes of Near-infrared Pre-main-sequence Sources

YSO	α_{2000} (^h ^m ^s)	δ_{2000} ([°] ['] ^{''})	J (mag)	H (mag)	K (mag)
NIR1	16:19:48.421	-49:38:13.39	16.02 ± 0.09	13.54 ± 0.04	12.23 ± 0.03
NIR2	16:19:48.693	-49:37:02.60	15.01 ± 0.07	14.46 ± 0.11	13.99 ± 0.08
NIR3	16:19:50.237	-49:37:28.78	15.70 ± 0.08	14.64 ± 0.09	13.94 ± 0.07
NIR4	16:19:51.425	-49:37:16.62	14.47 ± 0.05	13.84 ± 0.05	13.42 ± 0.06
NIR5	16:20:00.259	-49:36:27.51	14.69 ± 0.05	13.98 ± 0.05	13.58 ± 0.05
NIR6	16:20:01.816	-49:36:47.06	16.05 ± 0.09	14.58 ± 0.13	13.61 ± 0.08
NIR7	16:20:01.850	-49:36:20.02	15.35 ± 0.07	13.93 ± 0.07	13.07 ± 0.04
NIR8	16:20:03.207	-49:35:22.64	11.49 ± 0.02	11.31 ± 0.05	11.09 ± 0.06
NIR9	16:20:03.534	-49:36:01.26	16.07 ± 0.09	15.08 ± 0.13	14.33 ± 0.12
NIR10	16:20:03.731	-49:36:24.67	13.73 ± 0.03	13.24 ± 0.04	12.98 ± 0.04
NIR11	16:20:04.090	-49:36:30.99	13.10 ± 0.02	12.78 ± 0.04	12.52 ± 0.04
NIR12	16:20:04.112	-49:36:12.82	14.43 ± 0.02	13.99 ± 0.02	13.72 ± 0.05
NIR13	16:20:05.813	-49:35:19.74	13.13 ± 0.05	12.80 ± 0.04	12.63 ± 0.03
NIR14	16:20:06.003	-49:35:26.97	11.66 ± 0.03	11.35 ± 0.04	11.19 ± 0.03
NIR15	16:20:07.787	-49:35:26.88	16.48 ± 0.13	14.52 ± 0.06	13.28 ± 0.04
NIR16	16:20:08.299	-49:36:24.99	14.93 ± 0.04	14.33 ± 0.11	13.37 ± 0.14
NIR17	16:20:08.346	-49:35:55.60	12.98 ± 0.03	12.63 ± 0.06	12.38 ± 0.07
NIR18	16:20:08.824	-49:36:03.85	15.33 ± 0.19	13.38 ± 0.20	11.34 ± 0.07
NIR19	16:20:08.843	-49:36:30.29	14.09 ± 0.04	13.41 ± 0.07	12.85 ± 0.09
NIR20	16:20:09.049	-49:36:37.69	14.78 ± 0.04	14.15 ± 0.08	13.64 ± 0.08
NIR21	16:20:09.214	-49:35:05.28	12.66 ± 0.03	12.26 ± 0.05	11.74 ± 0.03
NIR22	16:20:09.456	-49:36:34.86	13.06 ± 0.03	12.53 ± 0.04	12.19 ± 0.05
NIR23	16:20:09.683	-49:36:01.66	12.24 ± 0.03	11.44 ± 0.06	10.82 ± 0.05
NIR24	16:20:09.836	-49:36:27.91	14.82 ± 0.13	14.24 ± 0.22	13.36 ± 0.12
NIR25	16:20:12.553	-49:36:44.04	14.83 ± 0.02	14.26 ± 0.07	13.57 ± 0.06
NIR26	16:20:14.118	-49:37:32.91	13.99 ± 0.02	13.63 ± 0.04	13.43 ± 0.05
NIR27	16:20:14.949	-49:37:17.82	14.04 ± 0.05	13.68 ± 0.05	13.39 ± 0.07
NIR28	16:20:15.384	-49:36:43.86	14.36 ± 0.09	13.88 ± 0.08	13.60 ± 0.07
NIR29	16:20:15.470	-49:36:51.72	13.82 ± 0.03	13.58 ± 0.06	13.40 ± 0.06
NIR30	16:20:15.827	-49:37:11.98	15.67 ± 0.08	14.34 ± 0.05	13.36 ± 0.06
NIR31	16:20:19.361	-49:34:58.80	11.25 ± 0.04	10.43 ± 0.04	9.91 ± 0.05
NIR32	16:20:22.523	-49:35:40.19	13.96 ± 0.02	13.55 ± 0.03	13.31 ± 0.03
NIR33	16:20:23.306	-49:35:46.32	14.72 ± 0.03	14.28 ± 0.05	14.01 ± 0.06
NIR34	16:20:27.642	-49:35:13.01	14.78 ± 0.04	14.24 ± 0.05	13.94 ± 0.05

10 km s⁻¹ for typical H II regions (Stahler & Palla 2005). R is the radius of the source. The estimated dynamical ages for S1 and S2 are found to be 0.2 and 0.01 Myr, respectively. This hints at the youth of S2 relative to S1. It is to be noted that the dynamical age has been calculated assuming a medium that is homogeneous and spherically symmetric. This is unlikely to represent the factual situation. Hence, t_{dyn} should be considered representative at best.

3.6. YSOs Associated with G333.73

Color excess at infrared wavelengths has been extensively used to identify the young objects and to broadly categorize them according to evolutionary stages. Recent studies in nearby star-forming regions have shown that the *Spitzer*-IRAC color-color diagrams are particularly useful in identifying the young stellar population in these regions, as the IRAC bands are highly sensitive to the emission from the circumstellar disks and envelopes (e.g., Allen et al. 2004; Megeath et al. 2004; Hartmann et al. 2005). Examining different models and combining them with the observations, they have found that the different classes of YSOs such as Class I (central source + disk + envelope) and Class II (central source + disk) objects occupy distinct regions in the color-color diagram. In addition to this, the color-color diagrams that combine the IRAC and

MIPS 24 μ m data are often used to identify highly embedded stars and sources with significant inner holes (e.g., Lada et al. 2006; Rho et al. 2006).

In order to study the YSO population within this IRDC, we searched the Glimpse I'07 Archive for mid-infrared point sources. For this, we have considered all sources lying within the 3σ contour of the 1.2 mm emission. By proceeding in this way, we attempt to identify sources associated with the IRDC and eliminate other field objects that are not related to G333.73. However, as the mid-infrared emission from S1 extends beyond the 3σ contour of the 1.2 mm emission, we have also considered sources within a circular region of radius 1'5 around S1 (centered at $\alpha_{J2000} = 16^{\text{h}}20^{\text{m}}09^{\text{s}}.4$, $\delta_{J2000} = -49^{\circ}36'21''$). Among these two groups of *Spitzer* sources, we find that 73 are detected in all four IRAC bands. We have also carried out a visual inspection of this region in all the IRAC images by scaling the images to identify sources embedded in mid-infrared nebulosity and find that 16 sources were not identified in the GLIMPSE catalog. Hence, we have performed aperture photometry on these sources using the task `qphot` in IRAF software. For this, we have selected a 5'' aperture. The inner and outer radii of the sky annulus are 6'' and 8'5, respectively. In order to identify the YSO candidates, we used the methods prescribed by Megeath et al. (2004) and Allen et al. (2004). For the sources detected in all IRAC bands, we employed the [5.8]–[8.0] versus

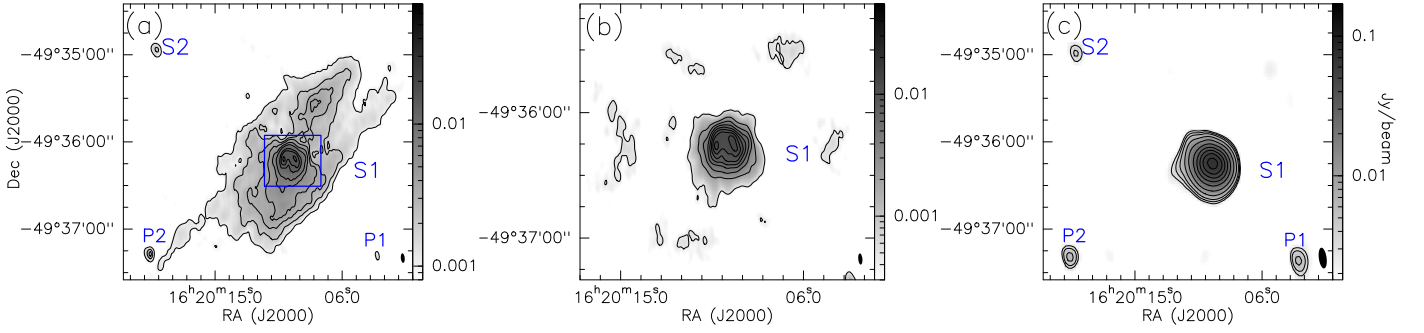


Figure 14. (a) Low-resolution radio continuum map of G333.73+0.37 at 1300 MHz. The contour levels are at 1.4, 2.1, 3.1, 4.1, 6.1, 8.1, 10.1, 12.1, 14.1, and 16.1 mJy beam⁻¹ with beam size of 6''6 × 2''7. The compact shell structure is enclosed within the rectangle. (b) High-resolution map of the rectangular region shown in panel (a). The contour levels are from 2 to 19 mJy beam⁻¹ in steps of 2.2 mJy beam⁻¹. The corresponding beam size is 5''5 × 2''0. (c) Radio continuum map of G333.73+0.37 at 610 MHz. The contour levels are from 3.5 to 98 mJy beam⁻¹ in steps of 10 mJy beam⁻¹. The corresponding beam size is 14''5 × 5''4. The beams are represented as filled ellipses toward the bottom right of all panels.

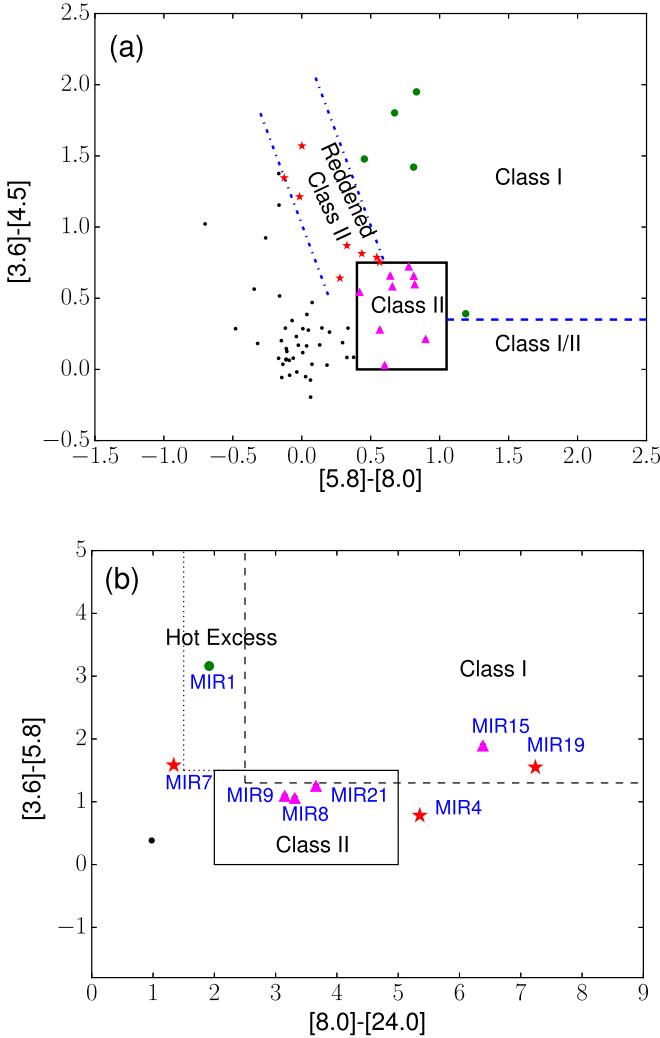


Figure 15. (a) *Spitzer*-IRAC color-color diagram using the colors [3.6]–[4.5] vs. [5.8]–[8.0]. The solid rectangle indicates the position occupied by Class II objects, while parallel dotted lines represent the region occupied by reddened Class II objects. The top right region of the color-color diagram is occupied by Class I sources, and the region to the right of Class II sources is occupied by Class I/II objects. Filled circles (green) represent Class I YSO candidates, and triangles (magenta) denote Class II objects. Reddened Class II objects are represented with a star symbol (red). Other sources are marked as filled circles (black). (b) Color-color diagram of [3.6]–[5.8] vs. [8.0]–[24.0] using mid-infrared magnitudes from *Spitzer*-IRAC and MIPS. The solid rectangle indicates the region occupied by Class II objects, whereas the region marked by dashed lines represents the region occupied by Class I objects. The dotted line indicates the location of “hot excess” sources (see text).

[3.6]–[4.5] color-color diagram to locate the YSO sources. The color-color diagram is shown in Figure 15(a). The regions occupied by Class I, Class II, and reddened Class II sources, based on the predictions of existing models for disks and envelopes (Megeath et al. 2004), are also shown in the image. A total of 22 YSO candidates are detected in the color-color diagram. Of these, five are Class I sources, nine are Class II sources, and eight are reddened Class II sources.

The 24 μ m data, if available, serve as an additional tool to discriminate between Class I and Class II objects. The SED of Class II objects is flat or declining near 24 μ m, whereas it is rising for Class I YSOs (Kerton et al. 2013). We have therefore employed the flux densities from the 24 μ m point-source catalog of Gutermuth & Heyer (2015) to plot the IRAC-MIPS color-color diagram. From the catalog, we have identified seven sources within both of our regions of interest. We again carry out a visual inspection of the MIPS 24 μ m image and find that there are five additional sources that are not listed in the catalog. We performed aperture photometry on these sources using the task *qphot* in IRAF. The parameters for the photometry are taken from Gutermuth & Heyer (2015). This leads to a total of 12 sources at 24 μ m. Of these, nine sources have IRAC magnitudes in all four bands. Among the 12, two sources whose photometry is carried out by us are detected only in the 24 μ m band. These sources are likely to be Class 0 protostellar objects, although we cannot exclude the possibility of these being background objects.

We have constructed a color-color diagram, [3.6]–[5.8] versus [8.0]–[24.0], based on IRAC and MIPS colors, which is used to identify the Class II and Class 0/I sources. This color-color diagram is shown in Figure 15(b). The Class I YSO MIR1 lies in the “hot excess” region and is of interest, as this region is occupied mostly by Herbig AeBe stars. Class II YSOs with large extinction ($A_V > 25$) or Class 0/I objects with an extra hot component from unusually active accretion can also fall in the “hot excess” region (Rho et al. 2006). The reddened Class II YSO MIR7 also lies just outside the boundary of “hot excess” objects. Object MIR4 lies in the region to the right of Class II objects. This source has a large [8.0]–[24.0] excess compared to [3.6]–[5.8] color. A visual inspection of MIR4 reveals that another YSO, designated MIR5 (Table 5), lies in close vicinity of this source (angular separation of 3''). Hence, the flux attributed to MIR4 in that catalog apparently has a contribution from MIR5 owing to resolution effects.

Even though we have identified the YSO population associated with this region using the mid-infrared color-color diagrams, not

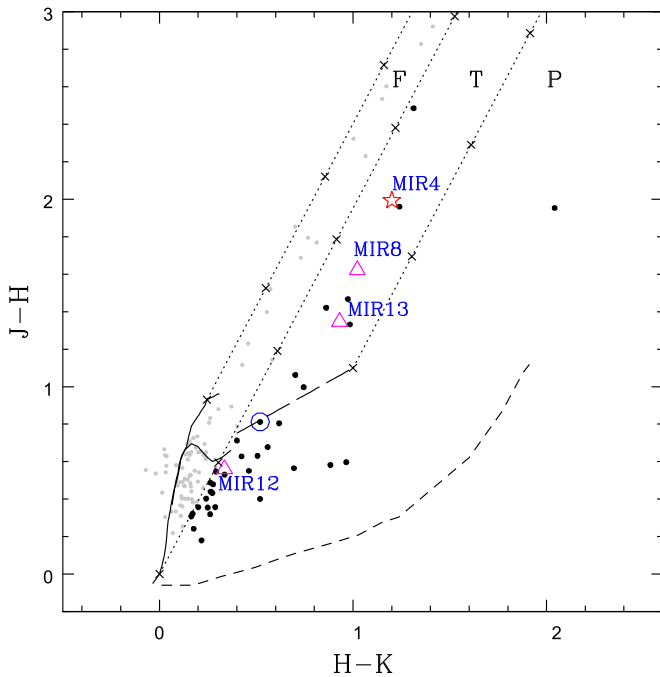


Figure 16. Color-color diagram of the 2MASS sources in the G333.73 region. The two solid curves represent the loci of giant (thick line) and main-sequence stars (thin line) derived from Bessell & Brett (1988). The classical T Tauri locus from Meyer et al. (1997) is represented with a long-dashed line. The parallel dotted lines are the reddening vectors, with crosses placed at intervals corresponding to 5 mag of visual extinction. We have assumed the interstellar reddening law of Rieke & Lebofsky (1985) ($A_I/A_V = 0.282$, $A_H/A_V = 0.175$ and $A_K/A_V = 0.112$). The short-dashed line represents the locus of the Herbig AeBe stars (Lada & Adams 1992). The plot is classified into “F,” “T,” and “P” regions (see text for details). The colors and the curves shown in the figure are transformed to the Bessell & Brett (1988) system. Sources that are classified as main sequence or giants are represented by gray dots, whereas pre-main-sequence sources are denoted by black dots. IRAC YSOs identified from the mid-infrared color-color diagram having 2MASS counterparts are also shown and labeled in the image. The circled dot denotes the central object corresponding to source S2.

all sources are detected in all four IRAC bands. This is due to the fact that the [3.6] and [4.5] bands are more sensitive compared to others (Fazio et al. 2004). Moreover, the [5.8] and [8.0] bands trace emission from PAHs that can confuse the detection and photometry of point sources. Hence, we have resorted to the near-infrared (NIR) Two Micron All Sky Survey (2MASS) ($H - K_s$) versus ($J - H$) color-color diagram to identify the young population of sources. We have selected sources with good photometric magnitudes (read flag = 2) that are detected in all three bands. A total of 127 sources are detected within both the regions described earlier. This color-color diagram, shown in Figure 16, is classified into three distinct regions (Sugitani et al. 2002; Tej et al. 2006). The “F” sources are located within the reddening bands of main-sequence and giant stars and are believed to be field stars, Class III objects, or Class II objects with small NIR excess. “T” sources occupy the region toward the left of the “F” region, and to the right of the reddening vector corresponding to the T Tauri locus. The sources in this region are mostly classical T Tauri stars (Class II) with large NIR excess, although there could be a few Herbig AeBe stars with small NIR excess. Toward the right of “T” is the “P” region, which is occupied by sources that are relatively younger (Class I or Herbig AeBe stars). From our sample, we find 38 sources that show NIR color excess (i.e., populating the “P” and “T” regions). The details

of these YSOs are listed in Table 6 with labels NIR1, NIR2, ..., NIR 38. Eleven sources fall in the “T” region and 27 in the “P” region. Among the YSOs identified in the NIR, four objects are already classified as Class II sources based on IRAC colors.

Figure 17 shows the distribution of all 56 YSO candidates identified in this region: 22 IRAC YSOs and 34 NIR YSO candidates. Nearly 80% of the YSOs detected solely using NIR colors are located in the proximity of S1. This is explicable, as the sources away from S1 along the length of the IRDC have a low probability of detection owing to higher extinction, also evident from the column density map. This YSO sample is limited by sensitivity and nebulousity. Hence, we would like to bring attention to the fact that this is a representative subsample of the total YSO population in this IRDC.

3.7. SED Modeling of YSOs

Subsequent to the identification of YSOs, we are interested in gaining an insight into their characteristics such as mass, evolutionary stage, stellar temperature, envelope accretion rate, and disk mass. To achieve this, we resort to the radiative transfer models of Robitaille et al. (2007) and use them to fit the SEDs of the YSOs. We have fitted SEDs of nine YSO candidates: MIR1, MIR4, MIR5, MIR7, MIR8, MIR9, MIR15, MIR19, and MIR21, whose $24 \mu\text{m}$ fluxes are known. The reason for selecting these sources for SED modeling is that the data at longer wavelengths, if available, serve as a better tool to constrain the models. For MIR4 and MIR5, only a single common flux density at $24 \mu\text{m}$ is at hand, and we use it as an upper limit for both these objects. In addition, we have selected a YSO identified based on NIR colors, NIR31, which is in close vicinity ($\sim 3''$) to the radio peak toward S2. Besides, the source is detected at 3.6 and $4.5 \mu\text{m}$ IRAC bands. It is also detected in the optical bands, and we have used the flux densities at B and R bands from the USNO catalog (Monet 1998) and the I -band from the DENIS catalog (Epchtein 1998) in the construction of the SED. As the $24 \mu\text{m}$ image is saturated, we have used the 12 and $22 \mu\text{m}$ fluxes from the *WISE* catalog (Cutri et al. 2012) as upper limits (owing to the poor resolution of these images). Some of the sources appear point-like in the *Herschel* far-infrared images at 70 and $160 \mu\text{m}$. For these sources, we have estimated the flux densities within circular apertures of radius $10''$ and $20''$, respectively. These apertures have been taken considering the radial profile of bright point-like sources in this region. For other YSOs, as well as other wavelengths, we have considered flux densities of the corresponding clumps as upper limits. The YSO MIR9 lies outside the 3σ threshold of the 1.2 mm map; hence, for this object we carried out the fitting for wavelengths up to $24 \mu\text{m}$. The SED fitting of the 10 YSOs described above has been carried out using the command line version of the SED fitting tool. The results are shown in Figure 18. The fitted parameters, along with ranges corresponding to the first 10 best-fit models, are given in Table 7.

From the best-fit models, the masses of all sources fall in the range $1.7 \leq M_* \leq 10.0$. This suggests that all these sources are intermediate- to high-mass objects. MIR1, the YSO that has been identified as IRAS 16161–4931 earlier, is the most massive one ($10 M_\odot$) according to the models. The ages of all the objects other than MIR8 are $\lesssim 2$ Myr, hinting at the youth of these sources. We have classified the YSO candidates based on their evolutionary stages using the method described by Robitaille et al. (2006). This classification scheme divides the sources into three broad

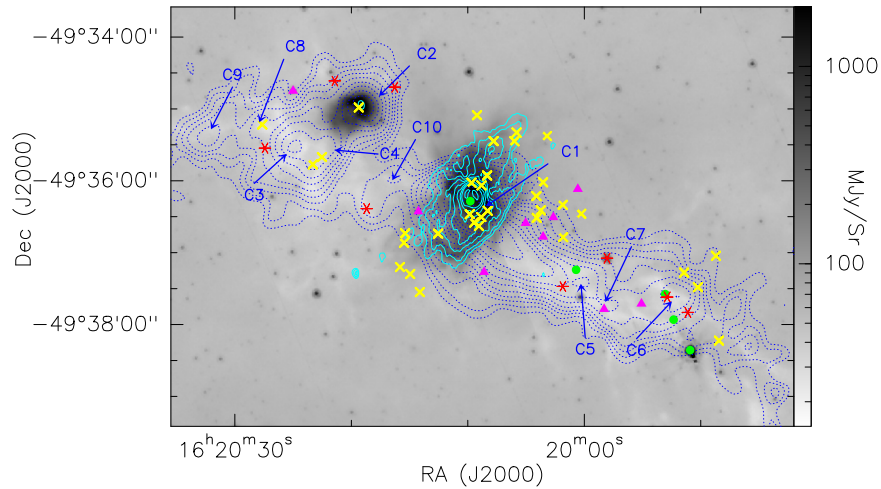


Figure 17. IRAC 8 μm image of the IRDC G333.73 overlaid with 1.2 mm cold dust contours (dotted) and low-resolution 1300 MHz contours (solid). Also marked in the image are the different classes of YSOs identified from NIR and mid-infrared color–color diagrams. IRAC Class I YSOs are denoted by filled circles (green), whereas Class II YSOs are marked as triangles (magenta). The asterisk (red) represents reddened Class II objects. Locations of the pre-main-sequence objects identified from the 2MASS color–color diagram are indicated by crosses (yellow). The 1.2 mm contour levels are from 40 to 1500 mJy beam^{-1} in steps of 70 mJy beam^{-1} . The 1300 MHz contour levels are the same as those shown in Figure 14(b). Also marked are the locations of the 10 mm clumps.

categories based on three physical properties: mass of the central object (M_*), envelope accretion rate (\dot{M}_{env}), and disk mass (M_{disk}). Stage 0/I objects are those with $\dot{M}_{\text{env}}/M_* > 10^{-6} \text{ yr}^{-1}$ and are believed to be objects with significant infalling envelopes and possibly disks. If $\dot{M}_{\text{env}}/M_* < 10^{-6} \text{ yr}^{-1}$ and $M_{\text{disk}}/M_* > 10^{-6}$, the object is classified as a Stage II source that has an optically thick disk and possible remains of an infalling envelope. If $\dot{M}_{\text{env}}/M_* < 10^{-6} \text{ yr}^{-1}$ and $M_{\text{disk}}/M_* < 10^{-6}$, it is a Stage III object with an optically thin disk. The advantage of using this classification scheme along with the classification based on the slope of infrared SED is that it can avoid possible confusion between observable and physical properties and thereby provides a more physical basis for YSO classification. Table 8 gives the values for \dot{M}_{env}/M_* and M_{disk}/M_* for the YSOs, including the classification based on different methods. We notice that M_{disk}/M_* corresponding to all 10 YSOs are above the threshold of 10^{-6} for having an optically thick disk, suggesting the fledgling nature of these objects.

According to the classification scheme of Robitaille et al. (2006), there is a single Stage I source, whereas there are five Stage I/II objects and four Stage II objects. We find that there is a broad corroboration between this classification scheme and those based on infrared colors. Two YSOs that show deviant behavior between the schemes are MIR1 and MIR7. From the SED modeling, we see that MIR1 and MIR7 fall into the Stage II category with zero envelope accretion rate. According to the IRAC color–color diagram, they are classified as Class I and Class II objects, respectively. But the IRAC-MIPS colors categorize them as “hot excess” objects. As mentioned earlier, these are suspected to be Class I sources or Class II objects with large extinction ($A_V > 25 \text{ mag}$). The extinctions estimated from the models are relatively large: 56 and 34 mag for MIR1 and MIR7, respectively. This is consistent with that predicted for a Class II object falling in the “hot excess” region. Hence, MIR1 and MIR7 are speculated to be Class II objects with large extinction. The ages of these sources are also relatively higher (1–4 Myr) compared to Stage I and I/II sources ($< 1 \text{ Myr}$). The object NIR31 that is associated with S2 is classified as a Stage I/II object from SED modeling and has

a mass of $\sim 7 M_\odot$. If radio emission from S2 is due to NIR31, we may be probing the radio emission from an intermediate YSO object. We explore this possibility later in Section 4.1.2. We would also like to point out that although we have applied these models for fitting the SEDs, the parameters are considered representative at best, as the models are based on assumptions that the SEDs of intermediate/massive YSOs are scaled-up versions of their lower-mass counterparts.

4. Discussion

In this section, we first discuss the active regions S1 and S2, to gain an insight into their morphologies and identify the likely sources of excitation. Thereafter, we probe the properties of the IRDC using various tracers to fathom the star formation potential of the cloud. Finally, we surmise about the evolutionary stage of the cloud itself based on various lifetime indicators.

4.1. Morphology of Radio Sources

4.1.1. S1

From the radio emission that traces the ionized gas (Figure 14), we perceive that S1 can be categorized as an H II region with a shell-like morphology. According to Wood & Churchwell (1989) and Kurtz et al. (1994), shell-like regions are the rarest (less than 5%) of all the H II regions detected. Recent studies of Sgr B2 and W49 star-forming regions (De Pree et al. 2005, and references therein) show a higher percentage of detection (28%) of shell-like H II regions. Strong stellar winds from the central OB stars, as well as the pressure from the ionizing radiation, are believed to induce the formation of shell-like/bubble structures in their vicinity (Weaver et al. 1977; Shull 1980). While radiation pressure on dust grains is capable of producing shell-like structures in ultracompact H II regions (Kahn 1974), they are generally less important compared to the stellar winds (Turner & Matthews 1984). An important probe of stellar winds is the presence or absence of extended 24 μm emission near the center of bubbles. The centrally peaked 24 μm favors the explanation that the grains are mostly heated by the absorption

Table 7
Parameters of the Models Shown in Figure 18

Source		χ^2	Mass (M_{\odot})	T_{eff} (K)	Luminosity (L_{\odot})	Inc. Angle (deg)	Env. Accretion Rate ($M_{\odot} \text{ yr}^{-1}$)	Disk Mass (M_{\odot})	A_V (mag)	Age (Myr)
MIR1 (IRAS 16161–4931)	Best fit	373.8	10.0	25790	6873.0	56.6	0	0.2	55.5	1.00
	Range	373.8–5122.0	7.7–10.3	21850–25790	2581.0–6873.0	31.8–75.5	0	$9.6 \times 10^{-3} - 0.3$	0–55.5	1.0–3.3
MIR4	Best fit	8.5	3.7	4847	30.3	81.4	1.1×10^{-5}	3.4×10^{-3}	7.2	0.38
	Range	8.5–14.7	3.7–5.3	4153–5945	14.9–31.8	56.6–81.4	$(0-2.4) \times 10^{-5}$	$4.3 \times 10^{-4} - 0.05$	3.3–13.1	0.08–2.2
MIR5	Best fit	3.6	4.0	6580	100.1	81.4	3.2×10^{-8}	1.3×10^{-4}	83.3	0.97
	Range	3.6–3.9	2.7–4.0	6580–12950	55.8–118.0	49.5–81.4	$(0-3.2) \times 10^{-8}$	$1.3 \times 10^{-4} - 0.05$	78.6–84.3	0.97–9.51
MIR7	Best fit	398.1	5.8	18020	1543.0	63.3	0	0.01	34.0	1.90
	Range	398.1–1267.0	4.6–6.4	15720–19240	84.2–1543.0	31.8–75.5	0	$3.3 \times 10^{-3} - 0.1$	28.2–34.0	1.53–4.38
MIR8	Best fit	33.6	3.1	12160	83.7	81.4	0	0.02	7.8	9.63
	Range	33.6–66.4	1.7–3.2	4335–12160	20.6–83.7	18.2–81.4	$(0-1.9) \times 10^{-6}$	$2.5 \times 10^{-3} - 0.02$	5.2–12.1	0.18–9.80
MIR9	Best fit	8.8	1.7	4401	15.4	18.2	2.7×10^{-6}	0.06	17.1	0.23
	Range	8.8–11.5	1.0–3.3	4134–4975	8.6–19.1	18.2–69.5	$6.3 \times 10^{-8} - 2.9 \times 10^{-6}$	$2.9 \times 10^{-5} - 0.06$	14.5–17.8	0.18–0.71
MIR15	Best fit	1.8	2.9	4385	66.8	81.4	8.6×10^{-5}	0.01	0	0.07
	Range	1.8–3.7	0.6–6.4	3793–4772	9.1–336.8	41.4–87.1	$3.5 \times 10^{-6} - 1.5 \times 10^{-3}$	$4.9 \times 10^{-5} - 0.17$	0–24.9	0.01–0.20
MIR19	Best fit	0.8	2.8	4542	36.5	81.4	1.2×10^{-5}	2.0×10^{-4}	5.6	0.18
	Range	0.8–2.4	2.7–5.6	4367–5950	36.5–221.0	49.5–87.1	$8.3 \times 10^{-6} - 1.5 \times 10^{-4}$	$2.0 \times 10^{-4} - 0.07$	0–20.9	0.05–0.31
MIR21	Best fit	50.8	5.6	4724	158.8	31.8	7.1×10^{-5}	0.02	29.3	0.14
	Range	50.8–83.8	4.3–5.6	4724–15130	137.8–408.4	18.2–81.4	$(0-7.1) \times 10^{-5}$	$1.2 \times 10^{-5} - 0.13$	20.1–29.6	0.14–1.92
NIR31 (S2)	Best fit	25.9	5.6	6462	267.0	18.2	1.3×10^{-6}	0.03	4.7	0.30
	Range	25.9–44.6	5.1–7.1	4445–6462	166.7–351.6	18.2–63.2	$1.3 \times 10^{-6} - 7.8 \times 10^{-4}$	$1.6 \times 10^{-5} - 0.15$	1.5–4.7	0.04–0.37

Note. Columns (4)–(9) give the mass, effective temperature, luminosity, inclination angle, envelope accretion rate, disk mass, extinction, and age, respectively. The parameters listed are for the best-fit model and the range of all 10 best fits.

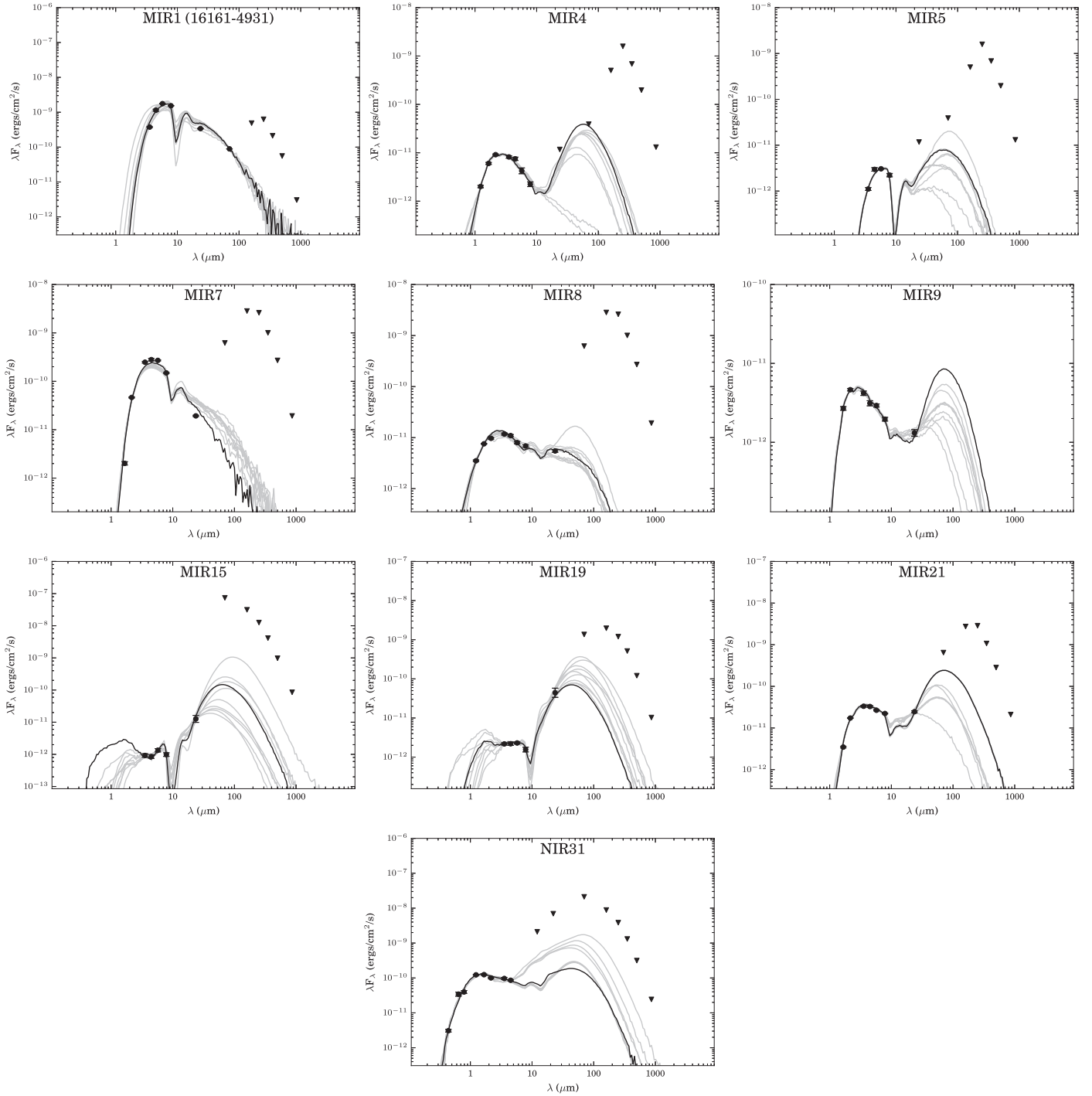


Figure 18. Infrared SEDs of YSO candidates MIR1, MIR4, MIR5, MIR7, MIR8, MIR9, MIR15, MIR19, and MIR21 and NIR source NIR31 fitted with the SED models of Robitaille et al. (2007). The filled circles represent input fluxes, and triangles represent upper limits in the far-infrared and submillimeter wavelengths. For NIR31, we have also given the fluxes in the optical bands (*B* and *R*). The best-fit model is shown as a black line, while the gray lines represent the subsequent nine good fits.

of Lyman continuum photons, which are abundant near the exciting star (Deharveng et al. 2010). In a few cases, a void is found to exist in the $24\ \mu\text{m}$ emission toward the center. This orifice could be either produced by stellar winds or due to the radiation pressure of the central star (Watson et al. 2008, 2009). Toward S1, we anticipate that the overall distribution of $24\ \mu\text{m}$ emission is similar to that of ionized gas, although the former is saturated toward the central region. This leads us to believe that

the stellar winds have not yet succeeded in clearing out dust from the central region. The emission at $24\ \mu\text{m}$ and radio is surrounded by an $8\ \mu\text{m}$ shell of enhanced emission. Toward the center, several high-extinction filamentary structures are perceived at $8\ \mu\text{m}$, evident from Figure 19(a).

We first explore the possibility of stellar winds from the central star being responsible for the observed shell-like morphology of the ionized gas. Note that the $8\ \mu\text{m}$ shell

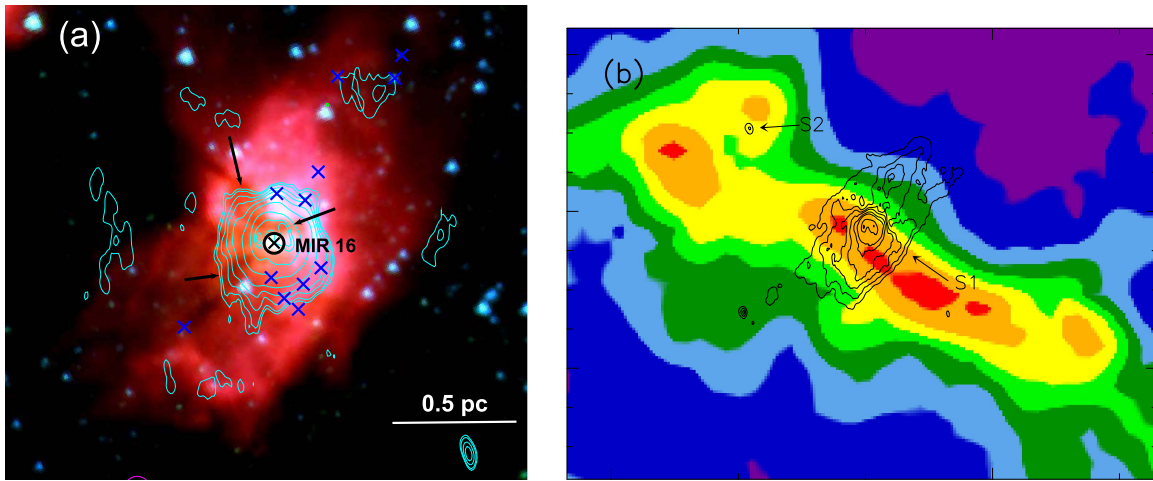


Figure 19. (a) *Spitzer*-IRAC color composite image of S1. Blue represents $3.6 \mu\text{m}$, green $4.5 \mu\text{m}$, and red $8 \mu\text{m}$. Radio emission at 1300 MHz is overlaid as cyan contours. All YSO candidates within the radio contours are marked as crosses. The location of the mid-infrared Class I object MIR16, which is at the center of the radio emission, is marked and labeled in the image. Arrows point toward high-extinction filamentary structures. (b) Smoothed column density map of G333.73 overlaid with 1300 MHz radio contours (black).

envelopes the ionized gas shell. The interaction of massive stellar winds with the ambient medium will sweep up dense shells of gas that expand away from the central source, and the swept-up shell(s) are exposed to the ionizing radiation from the newly formed star. This shell material may be partially or completely ionized, and the radius of the shell increases as a function of time. The radius (R_{shell}) and expansion velocity (V_{shell}) of the shell can be estimated using the following expressions (Castor et al. 1975; Garay & Lizano 1999):

$$R_{\text{shell}} = 0.042 \left(\frac{L_w}{10^{36} \text{ erg s}^{-1}} \right)^{1/5} \times \left(\frac{n_0}{10^5 \text{ cm}^{-3}} \right)^{-1/5} \left(\frac{t}{10^3 \text{ year}} \right)^{3/5} \text{ pc}, \quad (10)$$

$$V_{\text{shell}} = 24.7 \left(\frac{L_w}{10^{36} \text{ erg s}^{-1}} \right)^{1/5} \times \left(\frac{n_0}{10^5 \text{ cm}^{-3}} \right)^{-1/5} \left(\frac{t}{10^3 \text{ year}} \right)^{-2/5} \text{ km s}^{-1}, \quad (11)$$

where L_w is the mechanical luminosity of the stellar wind, n_0 is the density of the molecular cloud, and t is the shell expansion time. Based on the 1300 MHz radio image, the radius of the shell is taken as 0.05 pc. We adopt an archetypal shell expansion velocity of 10 km s^{-1} (e.g., Garay et al. 1986; Bloomer et al. 1998; Harper-Clark & Murray 2009) and consider the cloud density to be $1.6 \times 10^4 \text{ cm}^{-3}$. Using these values, we estimate the mechanical luminosity and shell expansion time to be $1.5 \times 10^{34} \text{ erg s}^{-1}$ and $2.9 \times 10^3 \text{ yr}$, respectively.

The expansion of the H II region could be due to the following: (i) the pressure difference between the ionized gas and ambient medium, or (ii) the stellar wind from the exciting star. A comparison of the expansion rates of both these mechanisms can aid in the determination of the stage of expansion, i.e., whether the stellar wind dominates the classical expansion or vice versa. From previous studies (Shull 1980; Garay & Lizano 1999), it is seen that the stellar wind is more

important when the following condition is satisfied:

$$\left(\frac{L_w}{10^{36} \text{ erg s}^{-1}} \right) > 0.33 \left(\frac{N_{\text{Lyc}}}{10^{49} \text{ s}^{-1}} \right)^{2/3} \left(\frac{n_0}{10^5 \text{ cm}^{-3}} \right)^{-1/3}. \quad (12)$$

Considering the N_{Lyc} estimated from radio flux, we estimate the right-hand side as $4.8 \times 10^{34} \text{ erg s}^{-1}$, which is nearly three times larger compared to the mechanical luminosity of stellar wind, $\sim 1.5 \times 10^{34} \text{ erg s}^{-1}$. This suggests that the effect of stellar wind is lower than that surmised from classical expansion. However, we would like to allude to the fact that the derived stellar wind luminosity is based on a typical expansion velocity of 10 km s^{-1} . If we increase V_{shell} to 20 km s^{-1} , L_w increases by an order of magnitude, to $1.2 \times 10^{35} \text{ erg s}^{-1}$. On the other hand, if we decrease V_{shell} to 5 km s^{-1} , L_w changes to $1.9 \times 10^{33} \text{ erg s}^{-1}$. Thus, the expansion velocity is a crucial parameter that decides the stage of expansion of the H II region.

We also detect a large-scale diffuse emission in the radio waveband associated with S1, which conforms to the morphology of emission from warm dust. The large-scale morphology of radio emission can be attributed to the density gradient where the H II region expands out toward regions of lower density (Israel 1978; Tenorio-Tagle 1979). Figure 19(b) shows the distribution of ionized gas with respect to the column density map. The large-scale radio emission is distributed nearly perpendicular to the long axis of the cloud, where the column density is high. This explains the expansion of ionized gas toward regions of lower density, i.e., toward the northwest and southeast, whereas toward the east and west of the radio peak it is constricted by the high-density gas, consistent with the champagne flow model.

To unravel the stars responsible for the ionized gas emission, we probe the region for the YSO population, particularly toward the geometric center (R.A. = $16^{\text{h}}20^{\text{m}}09^{\text{s}}.89$, decl. = $-49^{\circ}36'15''.32$) of the bubble/shell. The Lyman continuum flux predicts O9.5–B0 as the single ZAMS star exciting the shell. In this estimate, the diffuse emission is not taken into consideration. While we have been unable to detect any object at the geometric center (in NIR or mid-infrared), we have detected a Class I source, MIR16, close to the center (angular separation of $2''$). The lack of detection of any

Table 8
YSO Evolutionary Stages Based on IRAC Color–Color Diagram and Classification Scheme by Robitaille et al. (2006)

YSO	\dot{M}_{env}/M_*	$\dot{M}_{\text{disk}}/M_*$	Classification (IRAC CC Diagram)	Classification (SED Modeling)
MIR1 ^a	0	$9.3 \times 10^{-4} - 0.04$	Class I	Stage II
MIR4	$(0-6.5) \times 10^{-6}$	$8.1 \times 10^{-5} - 0.01$	Red Class II	Stage I or II
MIR5	$(0-1.2) \times 10^{-8}$	$3.3 \times 10^{-5} - 0.02$	Class I	Stage II
MIR ^a	0	$5.2 \times 10^{-4} - 0.02$	Red Class II	Stage II
MIR8	0	$7.8 \times 10^{-4} - 0.01$	Class II	Stage II
MIR9	$1.9 \times 10^{-8} - 2.9 \times 10^{-6}$	$8.8 \times 10^{-6} - 0.06$	Class II	Stage I or II
MIR15	$5.5 \times 10^{-7} - 2.5 \times 10^{-3}$	$7.6 \times 10^{-6} - 0.28$	Class II	Stage I or II
MIR19	$1.5 \times 10^{-6} - 5.6 \times 10^{-5}$	$3.6 \times 10^{-5} - 0.03$	Red Class II	Stage I
MIR21	$(0-1.7) \times 10^{-5}$	$2.1 \times 10^{-6} - 0.03$	Class II	Stage I or II
NIR31	$1.8 \times 10^{-7} - 1.5 \times 10^{-4}$	$2.2 \times 10^{-6} - 0.03$...	Stage I or II

Note.

^a Hot excess sources based on the MIPS-IRAC CC diagram.

Table 9
Classification of Clumps Based on Multiwavelength Signposts
of Star Formation

Clump No.	Radio Source	IRAC 8 μm Peak	MIPS 24 μm Source	Clump Activity	Evolutionary Stage
C1	✓	✓	Saturated	A/E	Type 2
C2	✓	✓	Saturated	A/E	Type 2
C3	X	X	X	Q	Type 1
C4	X	X	X	Q	Type 1
C5	X	X	X	Q	Type 1
C6	X	X	✓	I	Type 2
C7	X	X	✓	I	Type 2
C8	X	X	X	Q	Type 1
C9	X	X	X	Q	Type 1
C10	X	X	X	Q	Type 1

Note. Q—quiescent; I—intermediate; A—active; E—evolved based on Battersby et al. (2010); ✓—detection; X—nondetection.

source at the geometric center is probably due to the nebosity and high extinction in this region, reinforced by the high-extinction filamentary structures observed in the NIR and mid-infrared wavelength bands, visible in Figure 19(a). We cannot rule out the possibility of an ionizing source being deeply embedded in the filamentary structures. In addition, we detect ionized peaks around the shell with lower flux density at 1300 MHz, shown in Figure 19(a). This would suggest that the large-scale radio emission could be the result of multiple objects rather than a single ionizing source, although it is possible that this is the fragmented emission from the nebulous gas. We also detect six YSOs around the radio shell. The distribution of these objects around the radio shell is explicable on the basis of lower extinction and nebosity in these regions.

4.1.2. S2

In this subsection, we examine the morphology of the compact H II region S2 (see Figure 20), which is located toward the northeast of S1 and possesses an arc-like structure when viewed in the mid-infrared warm dust emission. Diffuse nebosity at lower flux levels in the mid-infrared, spanning a region $0.4 \times 0.3 \text{ pc}^2$, is directed away from the concave edge of the arc. This cometary-shaped object is oriented along the NW–SE direction (see Figure 20). At 24 μm , the emission is

saturated, and hence the distribution of emission is indecipherable. Such mid-infrared arc-shaped features have been observed toward other star-forming regions (e.g., Povich et al. 2008; Nandakumar et al. 2016) and could be attributed to (i) expansion of an H II region, (ii) bow shocks due to high-velocity stars (Povich et al. 2008), or (iii) dust or a bow wave (Ochsendorf et al. 2014). The radio emission toward S2 is compact but shows hints of extension toward the diffuse emission, affirming the cometary outlook of the warm dust emission. The radio emission peaks approximately midway on the arc. The YSO NIR31 is located $\sim 3''$ away from the radio peak. This source is classified as a pre-main-sequence star based on the NIR color–color diagram, as well as from the SED modeling. The mass of this object is estimated to be $5-7 M_\odot$, an intermediate-mass YSO. Radio emission has been detected from several low- and intermediate-mass YSOs and is ascribed to stellar winds (Panagia & Felli 1975; Martin 1996) or collimated ionized jets (Reynolds 1986). We look into the possibility of NIR31 being the ionizing source of S2.

We first consider the bow shock model as the origin of the mid- and far-infrared arc-shaped emission (e.g., France et al. 2007; Kobulnicky et al. 2016). Massive stellar objects with energetic winds generate strong shocks in the surrounding medium. If the relative motion between the star and ambient medium is large, the shock will be bent back around the star. For supersonic velocities, the ambient gas is swept up into an arc-shaped bow shock and has been observed around several massive objects (e.g., Peri et al. 2012, 2015). We use simple analytic expressions to calculate the shock parameters. For a star moving supersonically in the plane of the sky, the bow shock is expected to trace a parabola. The shock occurs at a stand-off distance R_0 from the star where the stellar wind momentum flux equals the ram pressure of the ambient medium. The stand-off distance in the thin shell limit can be calculated using the expression (Wilkin 1996)

$$R_0 = \sqrt{\frac{\dot{m}_* v_w}{4\pi \rho_a v_*^2}}. \quad (13)$$

Here \dot{m}_* is the stellar wind mass-loss rate, v_w is the wind's terminal velocity, ρ_a is the mass density of the ambient gas, and v_* is the relative velocity of the star through the medium. The stellar wind mass-loss rate (\dot{m}_*) and wind terminal velocity (v_w)

are calculated using the expressions (Mac Low et al. 1991)

$$\left(\frac{\dot{m}_*}{10^{-6} M_\odot \text{ yr}^{-1}} \right) = 2 \times 10^{-7} \left(\frac{L}{L_\odot} \right)^{1.25}, \quad (14)$$

$$\log \left(\frac{v_w}{10^8 \text{ cm s}^{-1}} \right) = -38.2 + 16.23 \log \left(\frac{T_{\text{eff}}}{\text{K}} \right) - 1.70 \left(\log \left(\frac{T_{\text{eff}}}{\text{K}} \right) \right)^2. \quad (15)$$

From the radio continuum emission we estimate the spectral type of the ionizing source as B0–B0.5. Considering a B0.5-type star, we have adopted luminosity $L = 1.1 \times 10^4 L_\odot$ and effective temperature $T_{\text{eff}} = 26, 200 \text{ K}$ (Panagia 1973). Using these values, we get $\dot{m}_* = 0.23 \times 10^{-7} M_\odot \text{ yr}^{-1}$ and $v_w = 1060 \text{ km s}^{-1}$. We can estimate mass density using the electron number density derived in Section 3.5, using the expression $\rho_d = \mu m_H n_e$, where $n_e = 1.3 \times 10^3 \text{ cm}^{-3}$. Here μ is the mean nucleus number per hydrogen atom, taken as 1.4, and m_H is the mass of the hydrogen atom. The distance between NIR31 and radio peak is 0.04 pc, which corresponds to 8251 au. Considering this as R_0 , we obtain the stellar velocity v_* as 6.2 km s^{-1} . Typical stellar velocities observed in bow shock regions are $\sim 10 \text{ km s}^{-1}$ (van Buren & Mac Low 1992; Nakashima et al. 2016), which is similar to our estimate. The arc-shaped emission is also symmetric around MIR31. Therefore, we suggest that the observed mid-infrared arc could be the result of a bow shock due to MIR31. The arc-shaped features resulting from the stellar wind bow shocks are also detected in far-infrared wavelengths (e.g., Cox et al. 2012; Decin et al. 2012). Density gradients present in the cloud can also affect the bow shock symmetries (Wilkin 2000).

The expansion of the HII region toward a low-density medium could result in a cometary or arc-shaped morphology. A close examination of the morphology of S2 in 70 and $160 \mu\text{m}$ bands reveals that the far-infrared dust emission also follows an arc-like morphology similar to that seen at mid-infrared wavebands. At longer wavebands, the resolution prohibits us from distinguishing the morphology of cold dust emission in detail. If the nebulosity (seen in mid- and far-infrared with an inkling in radio) is due to a local density gradient in this direction, we would expect the constriction of ionized flow by a high-density medium on the far side of the head or arc. By comparing the radio emission and column density distribution in Figure 19(b), we observe a local maxima in the column density toward the north of S2. As mentioned earlier, the radio emission is slightly extended toward south of the column density peak. Hence, density gradients might be responsible for the observed morphology of S2. Apart from pure bow shocks and density gradients, there are various hybrid models that incorporate the effects of stellar winds into existing models (e.g., Gaume et al. 1994; Arthur & Hoare 2006). Hence, it is also possible that the arc-like morphology of S2 is a combination of a bow shock and density gradient.

An alternate possibility that has been considered to justify the arc-shaped emission is the dust wave model (Ochsendorf et al. 2014). Here the cometary morphology is a consequence of the interaction of radiation pressure of the star with the dust carried along by the photoevaporative flow. In our case, the cometary structure in S2 is unlikely to be the outcome of a bow wave, as we do not perceive any bubble structure around S2.

4.2. Evolutionary Stages of Clumps

We next examine the star-forming properties of the clumps in the IRDC using our multiwavelength approach. We estimate the relative evolutionary stages of clumps based on the evolutionary sequence proposed by Chambers et al. (2009) and Battersby et al. (2010). According to Chambers et al. (2009), in an IRDC, the star formation begins with a quiescent clump, which evolves later into an active clump (containing enhanced $4.5 \mu\text{m}$ emission called “green fuzzy” and a $24 \mu\text{m}$ point source) and finally becomes a red (enhanced $8 \mu\text{m}$ emission) clump. Battersby et al. (2010) further modified this classification scheme by incorporating radio emission and suggesting that the red clumps are diffuse ones without associated millimeter peaks. They discuss four important star formation tracers: (1) quiescent clump (no signs of active star formation), (2) intermediate clumps that exhibit one or two signs of active star formation (such as shock/outflow signatures or $24 \mu\text{m}$ point source), (3) active clumps that exhibit three or four signs of active star formation (“green fuzzies,” $24 \mu\text{m}$ point source, UCH II region, or maser emission), and (4) evolved red clumps with diffuse $8 \mu\text{m}$ emission. Sánchez-Monge et al. (2013) also proposed an evolutionary sequence where clumps are classified as either Type 1 or Type 2 owing to their detection in infrared/millimeter images. A clump is classified as Type 2 if it has associated mid-infrared emission and as Type 1 in the absence of mid-infrared emission. Thus, the quiescent clumps are Type 2, whereas intermediate/active clumps are Type 1.

We have searched for MIPS $24 \mu\text{m}$ point sources associated with the clumps within a search radius of $10''$ from the peak position. We also sought the locations of masers in this region in the literature. We find that while there has been a search for the 22 GHz water maser and 6.7 GHz methanol maser (half-power beam widths of $7'$ and $3'3$) toward this star-forming region, the masers were not detected (Braz et al. 1989; Schutte et al. 1993; Walsh et al. 1997). Hence, we have used solely the radio and mid-infrared data to classify the clumps. The results are presented in Table 9. The columns in the table list the clump name, association with radio and $8 \mu\text{m}$ peaks, and $24 \mu\text{m}$ point source. Column (5) testifies to the clump activity (Q—quiescent, A—active, I—intermediate, E—evolved), and column (6) shows whether a clump is in the Type 1 or Type 2 evolutionary stage. Among the 10 clumps considered, two (C1 and C2) are active/evolved clumps, two (C6 and C7) are intermediate clumps, and the remaining eight are quiescent clumps. The two active/evolved (A/E) clumps, C1 and C2, have higher dust temperatures ($T_d > 20 \text{ K}$) compared to the other clumps. The molecular gas associated with C1 also shows evidence of protostellar infall. The star formation activity in C1 and C2 has already been discussed in previous sections, and these clumps correspond to the star-forming regions S1 and S2. For the intermediate clumps, clump C6 harbors two mid-infrared YSOs, MIR4 and MIR5, whereas clump C7 is associated with the YSO MIR8.

4.2.1. Star-forming Potential of Quiescent Clumps

We probe the dynamical state of the quiescent clumps by comparing their free-fall and dynamical timescales. The parameter free-fall time (τ_{ff}) is defined as the timescale on which an object will collapse into a point under its own gravity. We estimate the

free-fall time of the quiescent clumps using the expression

$$\tau_{\text{ff}} = \left(\frac{3\pi}{32G\rho} \right)^{1/2} = 3.4 \left(\frac{100}{n_{\text{H}_2}} \right)^{1/2} \text{ Myr}, \quad (16)$$

where ρ is the density of the molecular clump and n_{H_2} is the number density of H_2 molecules (Dobbs et al. 2014). The free-fall times of the six quiescent clumps are listed in Table 10, and they lie in the range 0.1–0.2 Myr. It is to be noted that the estimates of τ_{ff} are based on the current density of the cloud, and if the clump is undergoing collapse, then the initial free-fall times may not be the same as the present-day estimates.

The dynamical or crossing time τ_{dyn} , defined as the time required for the sound waves to cross the clump, can be estimated using the expression (Tan et al. 2006)

$$\tau_{\text{dyn}} = \left(\frac{R}{\sigma_{\text{obs}}} \right). \quad (17)$$

Here R is the radius of the clump and σ_{obs} is the velocity dispersion of the cloud. We estimate $\sigma_{\text{obs}} \sim 0.9 \text{ km s}^{-1}$ using the FWHM of the optically thin H^{13}CO^+ line. The dynamical times of the quiescent clumps are listed in column (4) of Table 10, and they lie in the range of 0.3–0.4 Myr. The free-fall and dynamical time estimates can be used to predict whether a clump is gravitationally stable or not. A clump becomes gravitationally unstable if $\tau_{\text{ff}} < \tau_{\text{dyn}}$ (e.g., Contreras et al. 2017; Sanhueza et al. 2017). To analyze the potential of collapse for these quiescent clumps, we specify the ratio $\tau_{\text{ff}}/\tau_{\text{dyn}}$, tabulated in column (5) of Table 10. All six quiescent clumps have $\tau_{\text{ff}}/\tau_{\text{dyn}} < 1$, and these are prone to gravitational collapse. We note that these are representative values, and a more rigorous analysis would entail high-resolution molecular line observations to gauge the dispersion velocity in each clump.

Under the assumption that the quiescent clumps undergo collapse, we analyze their potential to form high-mass stars. For this, we use the formulation of Svoboda et al. (2016) to find the mass of the most massive star (M_{max}), likely to form in the clump, using a Kroupa (2001) stellar initial mass function (IMF). M_{max} is estimated using the expression

$$M_{\text{max}} = 20 \left(\frac{\sigma_{\text{sf}} M_{\text{clump}}}{0.3 \times 1064 M_{\odot}} \right)^{1/1.3} M_{\odot}. \quad (18)$$

Here σ_{sf} is the star-forming efficiency in the clump, taken as 30% in the present work (Lada & Lada 2003). The estimated M_{max} for the six quiescent clumps are listed in Table 10. The mass estimates range from 2.9 to $10.4 M_{\odot}$. This suggests that all the quiescent clumps in this region have the potential to form intermediate-mass to massive stars.

4.3. Fragmentation in the Filamentary Cloud

From clumps, we move on to the expanse of the cloud in order to assimilate a larger picture of the IRDC. G333.73 is located in the fourth Galactic quadrant, where multiple giant molecular filaments (GMFs) are located. GMFs are tremendously long filamentary clouds (aspect ratio ~ 50 or larger) with lengths exceeding 100 pc. A recent study by Goodman et al. (2014) suggests that these GMFs, also designated as “bones,” can be used to constrain the spiral structure of the Milky Way. A number of bone-like filaments have been identified in our

Galaxy (e.g., Zucker et al. 2015; Wang et al. 2016). Large-scale PV diagrams (i.e., Galactic longitude vs. velocity) reveal that many of these GMFs have velocity structures consistent with or close to that of the Scutum-Centaurus arm (see Zucker et al. 2015; Li et al. 2016). For G333.73, based on its Galactic longitude (333.73) and LSR velocity of -33.2 km s^{-1} , we believe that the cloud is located in the interarm region, closer to the Scutum-Centaurus arm in comparison to the Sagittarius-Carina arm (Abreu-Vicente et al. 2016). The smaller size ($\sim 7 \text{ pc}$) and aspect ratio (~ 5) of G333.73 suggest that this filament is unlikely to be a GMF itself. This is corroborated by studies where star formation in nearby molecular clouds has demonstrated that the distribution of gas and dust is often filamentary, comprising either a single filament or a network of filaments. These are believed to trace the densest regions of GMFs (Haikala et al. 2005; Myers 2009; Contreras et al. 2016). Recent surveys have found hundreds of filaments using *Herschel* and ATLASGAL (Schisano et al. 2014; Li et al. 2016). These filaments have lengths in the range of 1–30 pc and typical aspect ratios ~ 2 –30 and are dense ($N(\text{H}_2) \sim 10^{21}$ – 10^{22} cm^{-2}) and massive (100 – $10^5 M_{\odot}$). The size, aspect ratio, mass ($4700 M_{\odot}$), and average column density ($\sim 2.4 \times 10^{22} \text{ cm}^{-2}$) of G333.73 fall well within the range of values observed for other filamentary clouds.

We next compare the clump properties with those expected from the theoretical predictions of fragmentation of a filamentary cloud. Assuming that the clumps are governed by Jeans instability, we estimate the Jeans length of the homogeneous gas using the expression (Carroll & Ostlie 1996; Wang et al. 2014)

$$\lambda_{\text{J}} = c_s \left(\frac{\pi}{G\rho} \right)^{1/2} = 0.066 \left(\frac{T}{10 \text{ K}} \right)^{1/2} \left(\frac{n}{10^5 \text{ cm}^{-3}} \right)^{-1/2} \text{ pc}, \quad (19)$$

where G is the gravitational constant and c_s is the sound speed, T is the temperature of the clump, and n is the number density. The expression for Jeans mass is given as

$$M_{\text{J}} = \frac{\pi^{5/2} c_s^3}{6 \sqrt{G^3 \rho}} = 0.877 \left(\frac{T}{10 \text{ K}} \right)^{3/2} \left(\frac{n}{10^5 \text{ cm}^{-3}} \right)^{-1/2} M_{\odot}. \quad (20)$$

Employing average values of (i) temperature $\sim 16.8 \text{ K}$ and (ii) number density $\sim 3.6 \times 10^4 \text{ cm}^{-3}$ of the clumps in this region (Section 3.2), we determine $\lambda_{\text{J}} \sim 0.2 \text{ pc}$ and $M_{\text{J}} \sim 3.3 M_{\odot}$. Observationally, the radii of the clumps are found to lie between 0.3 and 0.9 pc, while the clump masses range from 87 to $1530 M_{\odot}$. The radii of these clumps are consistent with the calculated Jeans length, whereas the masses are larger by a factor of $\gtrsim 25$ compared to the Jeans mass. The thermal pressure by itself predicts a smaller Jeans mass than the observed clump masses, suggesting the dominance of turbulence in this region. This supports the idea that turbulence achieves greater significance in high-mass star-forming regions (Lada et al. 2008). As the molecular line width could have contributions from both thermal and nonthermal components, it is possible to estimate the magnitude of each of these effects. The mean thermal broadening can be calculated using the equation $V_{\text{therm}} = \sqrt{k T_{\text{ex}} / \mu m_{\text{H}_2}}$ and is found to be $\sim 0.2 \text{ km s}^{-1}$ for the average clump temperature. This is nearly a factor of

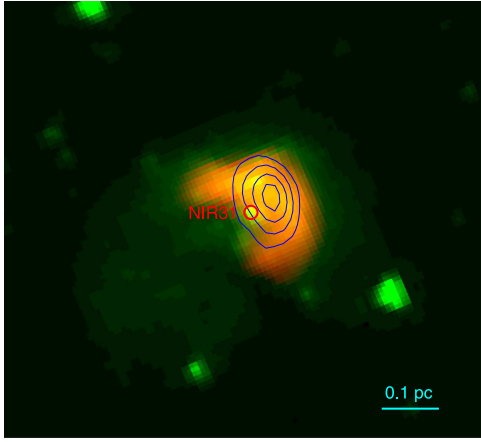


Figure 20. *Spitzer*-IRAC color composite image of S2. The $4.5\ \mu\text{m}$ emission is shown in green, and $8\ \mu\text{m}$ emission is in red. The circle marks the YSO source NIR31. The high-resolution radio map at 1300 MHz is overlaid as blue contours. Contour levels are the same as those of Figure 14(b).

four lower than the mean velocity dispersion of $0.9\ \text{km s}^{-1}$, implying the supersonic nature of the filament.

The clumps in G333.73 appear to be spaced regularly along the filament. The fragmentation along the filaments can be explained using the “sausage instability” model (Chandrasekhar & Fermi 1953), which can approximate a filamentary cloud to an isothermal cylinder. The self-gravitating cylinder in equilibrium has a critical linear mass density above which it will undergo gravitational collapse. If the turbulent pressure dominates over thermal pressure, the critical linear mass density is given by the expression (Jackson et al. 2010)

$$(M/l)_{\text{crit}} = 84\ \Delta V^2\ M_{\odot}\ \text{pc}^{-1}. \quad (21)$$

For $\Delta V = 2.2\ \text{km s}^{-1}$, $(M/l)_{\text{crit}}$ is found to be $\sim 407\ M_{\odot}\ \text{pc}^{-1}$, whereas the linear mass density of G333.73 is $(4700/7.2) \sim 653\ M_{\odot}\ \text{pc}^{-1}$. We observe that this exceeds the critical limit, and hence the cloud may be on the verge of global collapse. This is consistent with the infall motion seen in clump C1 (Section 3.3.3), as well as accretion signatures observed on a larger scale (next section). The presence of YSOs (André et al. 2010) and massive star formation (Li et al. 2016) substantiates the supercritical nature of the filamentary cloud.

4.4. Velocity Gradient in G333.73: Rotation or Accretion?

As discussed in Section 3.3.4, we have detected a fairly regular velocity gradient across the length of the filament. We first investigate whether this gradient could be a result of cloud rotation and estimate the ratio of rotational to gravitational energies, β , for a cylindrical cloud using the expression (Jiménez-Serra et al. 2014, and references therein)

$$\beta = \frac{E_{\text{rot}}}{E_{\text{grav}}} \sim \frac{\Omega^2 L^3}{36 G M} \sim \frac{V_{\text{grad}}^2 L}{36 G M}. \quad (22)$$

Here E_{grav} is the gravitational energy of the cylindrical cloud given by $E_{\text{grav}} = 3/2 G M^2/L$ for a cloud of mass M and length L , and G is the gravitational constant. E_{rot} is the kinetic energy due to the cloud’s rotation, defined as $E_{\text{rot}} = \frac{1}{2} I \Omega^2$, where Ω is the angular speed of the cloud and I is the moment of inertia given as $I \sim \frac{M L^2}{12}$ when the rotational axis is perpendicular to the

long axis of the cylinder. Ω is estimated using the velocity gradient V_{grad} across the length, V_{grad}/L . For the case of G333.73, we consider $M \sim 4700\ M_{\odot}$, $L \sim 7.2\ \text{pc}$ and $V_{\text{grad}} \sim 5/7.2 \sim 0.7\ \text{km s}^{-1}\ \text{pc}^{-1}$. This gives $\Omega \sim 2.3 \times 10^{-14}\ \text{s}^{-1}$ and $\beta \sim 0.3$. Ragan et al. (2012) cite a value of $\beta \sim \frac{1}{3}$ as the breakup speed for rotating clouds, with larger values of β preventing cloud fragmentation and star formation. Our value of β is close to the breakup speed. However, this value is estimated using gradients from relatively low density tracers (^{13}CO) that can be dominated by turbulent motions (Arquilla & Goldsmith 1986; Goodman et al. 1993). This is also in accordance with what is observed by us. Therefore, our estimation of $\beta \sim 0.3$ using ^{13}CO is plausibly an overestimate. The presence of clumps as evidence of fragmentation suggests that any contribution of rotation to the velocity gradient is likely to be negligible.

An alternate scenario to explain the velocity gradient is accretion flows along the filament (Tobin et al. 2012; Smith et al. 2013). Under this presumption, we estimate the gas accretion rate along the filament (\dot{M}) considering a simple cylindrical model (Kirk et al. 2013) using the following expression:

$$\dot{M} = \frac{V_{\text{grad}} M}{\tan(\alpha)}. \quad (23)$$

Here α represents the angle of inclination of the long axis of the cylinder with respect to the plane of the sky. A value of $\alpha \sim 0^\circ$ would prohibit the detection of the velocity gradient, whereas $\alpha \sim 90^\circ$ would prevent the cylindrical cloud from appearing elongated to us. Taking an average value of $\alpha \sim 45^\circ$, we find the accretion rate to be $4.6 \times 10^{-3}\ M_{\odot}\ \text{yr}^{-1}$. This accretion rate is similar to those found in other star-forming regions (e.g., Galván-Madrid et al. 2009; Jiménez-Serra et al. 2014). We therefore believe that the accretion flows can reasonably explain the large-scale velocity gradient found in G333.73, rather than rotation. The findings support the infall motion observed in the high-density gas tracers and supercritical linear mass density derived earlier. However, we cannot rule out the residual effect of velocity coherence that has been widely observed in GMFs (Ragan et al. 2014; Wang et al. 2015).

4.5. Age Limit of the IRDC

After examining the global traits of G333.73, our motivation is to uncover a limit to the age of the IRDC based on our multiwavelength analysis. The fragmentation of the cloud to clumps and the level of star-forming activity within should permit us to ascertain the broad evolutionary state of the IRDC (Jackson et al. 2010). The dark quiescent filaments prior to the hot-core phase are believed to be in the earliest stages (Carey et al. 2000; Wang et al. 2014). The IRDCs that harbor young H II regions are likely to be in the intermediate phase (Xu et al. 2016, 2017). Thereafter, the H II regions evolve with time and disperse the IRDC, leading to the emergence of the embedded cluster, which reveals the active sites of massive star formation such as Orion and NGC 6334. Since G333.73 is associated with clumps that harbor H II regions and YSOs, it is consistent with the proposition that IRDCs are the precursors of massive star clusters and can form multiple high-mass stars simultaneously. The expanding H II region in G333.73 is in the process of dispersing the natal cloud in its immediate vicinity (Figure 19(b)).

Table 10
Properties of the Three Quiescent Clumps

Clump No.	M_{\max} (M_{\odot})	τ_{ff} (Myr)	τ_{dyn} (Myr)	$\tau_{\text{ff}}/\tau_{\text{dyn}}$
C3	10.4	0.2	0.4	0.5
C4	9.7	0.2	0.4	0.5
C5	8.5	0.2	0.4	0.5
C8	2.9	0.2	0.3	0.7
C9	10.3	0.2	0.4	0.5
C10	8.6	0.1	0.3	0.3

Therefore, we believe that G333.73 is in an intermediate phase as compared to prestellar filamentary clouds and highly evolved regions that harbor massive star clusters in our Galaxy.

In this work, we presented different timescales such as the age of the H II region, the age of YSOs from SED modeling, and free-fall and dynamical timescales of the clumps. We now compare these estimates and attempt to derive a limit for the current age of G333.73. The expansion timescales of the compact H II regions S1 and S2 are found to be 0.2 and 0.01 Myr, respectively. We also estimated the free-fall and dynamical times of the quiescent clumps, which lie within the range of 0.1–0.4 Myr. The ages of YSOs in this region, based on the best fit to the SED using radiative transfer models, fall in the range of 0.1–9.6 Myr. All the YSOs except one (MIR8) are younger than 2 Myr according to the best-fit models. For MIR8, we find that the lower limit to the age among 10 best-fit models is 0.2 Myr. If we consider the YSOs other than MIR8, we could assign a lower limit to the age of G333.73 of 2 Myr. The ages of giant molecular clouds (GMCs) are usually estimated to be nearly two to three times the free-fall timescale (Murray 2011). The free-fall times of GMCs are estimated using a mean cloud density, based on the CO emission density that is converted directly to a hydrogen column density assuming a constant CO-to-H₂ abundance ratio (e.g., Scoville & Solomon 1975; Gordon & Burton 1976; Sodroski 1991). We estimated the mean CO density of the cloud from our CO maps and find $n(\text{H}_2) \sim 2300 \text{ cm}^{-3}$. This corresponds to $\tau_{\text{ff}}^{\text{cloud}} \sim 0.7 \text{ Myr}$, giving an age estimate of $\sim 2 \text{ Myr}$. This is in conformity with those obtained by other means. However, a caveat is that we are sampling the relatively higher density region of the cloud, and it may not be prudent to use these densities to obtain a measure of the limit to the age of the cloud.

We reform our goal to estimate the age of the clumps, as that can provide a lower limit to the age of the IRDC. In order to carry this out, we refer to the characteristic timescales occupied by the starless and star-forming phases in a cloud. Battersby et al. (2017) carried out a pixel-by-pixel analysis of the cloud complex within a $2^\circ \times 2^\circ$ of the Galactic plane and noticed that the starless phase occupies nearly 60%–70% of the dense molecular region (DMR) lifetime while the star-forming phase is approximately 30%–40% of the total DMR lifetime. The total lifetime of DMRs τ_{tot} based on the association with ultracompact H II regions (UCH II) is given by the following expression (Battersby et al. 2017):

$$\tau_{\text{tot}} = \frac{\tau_{\text{UCH II}}}{f_{\text{star}} f_{\text{UCH II}}}, \quad (24)$$

where $\tau_{\text{UCH II}}$ is the age of the UCH II region, f_{star} is the fraction of starry pixels, and $f_{\text{UCH II}}$ is the fraction of pixels that are associated with UCH II regions. We apply the above expression

to clumps themselves in order to secure a limit to the age. Based on our clump analysis, we demonstrated that four clumps are in the star-forming phase (i.e., active, evolved, and intermediate) and the remaining six are in the quiescent phase. This gives us the fraction of starry clumps as 40%. Of the four star-forming clumps, two harbor compact H II regions that lead us to $f_{\text{UCH II}} \sim 50\%$. $\tau_{\text{UCH II}}$ is taken as 0.2 Myr, considering the H II region expansion timescale of S1 estimated in Section 3.5. This is in agreement with the age of ultracompact H II regions from chemical clocks (Treviño-Morales et al. 2014). We then estimate a lower limit to the lifetime of G333.73 as 1 Myr. This is consistent with the absolute lifetime estimate of Battersby et al. (2017) for massive star-forming clouds, which is 1–3 Myr. We also obtained a similar estimate based on the age of YSOs. Hence, the age of G333.73 is likely to be 1–2 Myr. An upper limit could be the lifetimes of GMCs in our Galaxy, which is found to lie between 10 and 20 Myr (Murray 2011; Dobbs et al. 2014), although GMFs are expected to be older (Duarte-Cabral & Dobbs 2017).

5. Conclusion

In this work, we present the continuum and molecular line study of the filamentary IRDC G333.73. The results are summarized as follows.

(i) G333.73 is an IRDC with filamentary morphology at a distance of 2.6 kpc with a spatial extent of $7.2 \times 1.5 \text{ pc}$. Mid-infrared images reveal the presence of two bright sources, S1 and S2, connected by high-extinction structures. S1 is a bubble, and S2 has an arc-like structure.

(ii) Far-infrared and submillimeter emission is detected toward G333.73. We detect 10 cold dust clumps in this region. The temperature of the clumps ranges between 14.3 and 22.3 K, with the peak located toward S1. The column density map exhibits multiple peaks coinciding with the locations of high-density clumps. The total mass of this IRDC is estimated to be $4700 M_{\odot}$.

(iii) Eight molecular species (HCO^+ , H^{13}CO^+ , HCN, HNC, N_2H^+ , C_2H , ^{12}CO , and ^{13}CO) are detected in this IRDC. The profiles of HCN and HNC molecules toward S1 exhibit signatures of protostellar infall. We also detect a fairly steady velocity gradient along the major axis of the filament. The observed gradient is explained using accretion flows along the filament.

(iv) Low-frequency radio emission is detected toward S1 and S2 at 1300 and 610 MHz. S1 is associated with a shell-like H II region, whereas S2 is a compact source. Assuming a single ZAMS exciting star in each region, the spectral types of these sources are consistent with late O or early B type stars. The expansion timescales of H II regions associated with S1 and S2 are 0.2 and 0.01 Myr, respectively.

(v) We detected a total of 56 YSOs in different evolutionary stages within the IRDC. The radiative transfer modeling of 10 sources having $24 \mu\text{m}$ counterparts suggests that these are intermediate- to high-mass objects.

(vi) The G333.73 filament is supercritical and harbors multiple objects in different evolutionary stages such as millimeter cores, H II regions, and YSOs. A lower limit to the age of the IRDC is estimated as 1–2 Myr.

We are grateful to the referee for the valuable comments and insights that significantly improved the quality of this paper. We thank the staff of GMRT, who made the radio observations

possible. GMRT is run by the National Centre for Radio Astrophysics of the Tata Institute of Fundamental Research. Thanks are also due to R. Cesaroni for providing the 1.2 mm map of this region. This research made use of NASA/IPAC Infrared Science Archive, which is operated by the Jet Propulsion Laboratory, Caltech, under contract with NASA. This publication also made use of data products from *Herschel* (ESA space observatory). A.S.-M. is partially supported by the Collaborative Research Centre SFB 956, subproject A6, funded by the Deutsche Forschungsgemeinschaft (DFG).

ORCID iDs

Á. Sánchez-Monge  <https://orcid.org/0000-0002-3078-9482>

References

- Abreu-Vicente, J., Ragan, S., Kainulainen, J., et al. 2016, *A&A*, **590**, A131
- Allen, L. E., Calvet, N., D'Alessio, P., et al. 2004, *ApJS*, **154**, 363
- Anderson, L. D., Zavagno, A., Deharveng, L., et al. 2012, *A&A*, **542**, A10
- André, P., Men'shchikov, A., Bontemps, S., et al. 2010, *A&A*, **518**, L102
- Arquilla, R., & Goldsmith, P. F. 1986, *ApJ*, **303**, 356
- Arthur, S. J., & Hoare, M. G. 2006, *ApJS*, **165**, 283
- Barnes, P. J., Muller, E., Indermuehle, B., et al. 2015, *ApJ*, **812**, 6
- Battersby, C., Bally, J., Ginsburg, A., et al. 2011, *A&A*, **535**, A128
- Battersby, C., Bally, J., Jackson, J. M., et al. 2010, *ApJ*, **721**, 222
- Battersby, C., Bally, J., & Svoboda, B. 2017, *ApJ*, **835**, 263
- Beltrán, M. T., Brand, J., Cesaroni, R., et al. 2006, *A&A*, **447**, 221
- Benjamin, R. A., Churchwell, E., Babler, B. L., et al. 2003, *PASP*, **115**, 953
- Bergin, E. A., & Langer, W. D. 1997, *ApJ*, **486**, 316
- Berry, D. S. 2015, *A&C*, **10**, 22
- Bessell, M. S., & Brett, J. M. 1988, *PASP*, **100**, 1134
- Beuther, H., Linz, H., Tackenberg, J., et al. 2013, *A&A*, **553**, A115
- Beuther, H., Ragan, S. E., Johnston, K., et al. 2015, *A&A*, **584**, A67
- Beuther, H., Semenov, D., Henning, T., & Linz, H. 2008, *ApJL*, **675**, L33
- Beuther, H., & Sridharan, T. K. 2007, *ApJ*, **668**, 348
- Bloomer, J. D., Watson, D. M., Pipher, J. L., et al. 1998, *ApJ*, **506**, 727
- Braz, M. A., Gregorio-Hetem, J. C., Scalise, E., Jr., Monteiro Do Vale, J. L., & Gaylard, M. 1989, *A&AS*, **77**, 465
- Bronfman, L., Nyman, L.-A., & May, J. 1996, *A&AS*, **115**, 81
- Busquet, G., Estalella, R., Palau, A., et al. 2016, *ApJ*, **819**, 139
- Busquet, G., Zhang, Q., Palau, A., et al. 2013, *ApJL*, **764**, L26
- Carey, S. J., Feldman, P. A., Redman, R. O., et al. 2000, *ApJL*, **543**, L157
- Carey, S. J., Noriega-Crespo, A., Mizuno, D. R., et al. 2009, *PASP*, **121**, 76
- Carroll, B. W., & Ostlie, D. A. 1996, *An Introduction to Modern Astrophysics* (Cambridge: Pearson)
- Castor, J., McCray, R., & Weaver, R. 1975, *ApJL*, **200**, L107
- Caux, E., Bottinelli, S., Vastel, C., & Glorian, J. M. 2011, in *IAU Symp. 280, The Molecular Universe*, ed. J. Cernicharo et al. (Cambridge: Cambridge Univ. Press), **120**
- Chambers, E. T., Jackson, J. M., Rathborne, J. M., & Simon, R. 2009, *ApJS*, **181**, 360
- Chandrasekhar, S., & Fermi, E. 1953, *ApJ*, **118**, 116
- Charnley, S. B. 1997, *MNRAS*, **291**, 455
- Chira, R.-A., Smith, R. J., Klessen, R. S., Stutz, A. M., & Shetty, R. 2014, *MNRAS*, **444**, 874
- Churchwell, E., Smith, L. F., Mathis, J., Mezger, P. G., & Huchtmeier, W. 1978, *A&A*, **70**, 719
- Codella, C., Bachiller, R., Nisini, B., Saraceno, P., & Testi, L. 2001, *A&A*, **376**, 271
- Compiègne, M., Flagey, N., Noriega-Crespo, A., et al. 2010, *ApJL*, **724**, L44
- Contreras, Y., Garay, G., Rathborne, J. M., & Sanhueza, P. 2016, *MNRAS*, **456**, 2041
- Contreras, Y., Rathborne, J. M., Guzman, A., et al. 2017, *MNRAS*, **466**, 340
- Cox, N. L. J., Kerschbaum, F., van Marle, A.-J., et al. 2012, *A&A*, **537**, A35
- Csengeri, T., Weiss, A., Wyrowski, F., et al. 2016, *A&A*, **585**, A104
- Cutri, R. M., Wright, E. L., Conrow, T., et al. 2012, *yCat*, **2311**
- Cyganowski, C. J., Brogan, C. L., Hunter, T. R., Churchwell, E., & Zhang, Q. 2011, *ApJ*, **729**, 124
- Dame, T. M., Hartmann, D., & Thaddeus, P. 2001, *ApJ*, **547**, 792
- Davis, C. J., Kumar, M. S. N., Sandell, G., et al. 2007, *MNRAS*, **374**, 29
- Decin, L., Cox, N. L. J., Royer, P., et al. 2012, *A&A*, **548**, A113
- Deharveng, L., Schuller, F., Anderson, L. D., et al. 2010, *A&A*, **523**, A6
- De Pree, C. G., Wilner, D. J., Deblasio, J., Mercer, A. J., & Davis, L. E. 2005, *ApJL*, **624**, L101
- Dobbs, C. L., Krumholz, M. R., Ballesteros-Paredes, J., et al. 2014, in *Protostars and Planets VI*, ed. H. Beuther et al. (Tucson, AZ: Univ. Arizona Press), **3**
- Duarte-Cabral, A., & Dobbs, C. L. 2017, *MNRAS*, **470**, 4261
- Dyson, J. E., & Williams, D. A. 1980, *Physics of the Interstellar Medium* (New York: Halsted Press)
- Egan, M. P., Shipman, R. F., Price, S. D., et al. 1998, *ApJL*, **494**, L199
- Epchtein, N. 1998, in *IAU Symp. 179, New Horizons from Multi-Wavelength Sky Surveys*, ed. B. J. McLean et al. (Dordrecht: Springer), **106**
- Fazio, G. G., Hora, J. L., Allen, L. E., et al. 2004, *ApJS*, **154**, 10
- Foster, J. B., Jackson, J. M., Barnes, P. J., et al. 2011, *ApJS*, **197**, 25
- France, K., McCandliss, S. R., & Lupu, R. E. 2007, *ApJ*, **655**, 920
- Fuller, G. A., Williams, S. J., & Sridharan, T. K. 2005, *A&A*, **442**, 949
- Galván-Madrid, R., Keto, E., Zhang, Q., et al. 2009, *ApJ*, **706**, 1036
- Garay, G., & Lizano, S. 1999, *PASP*, **111**, 1049
- Garay, G., Rodriguez, L. F., & van Gorkom, J. H. 1986, *ApJ*, **309**, 553
- Gaume, R. A., Fey, A. L., & Claussen, M. J. 1994, *ApJ*, **432**, 648
- Giannetti, A., Brand, J., Sánchez-Monge, Á., et al. 2013, *A&A*, **556**, A16
- Genard, D., González-García, M., Fuente, A., et al. 2012, *A&A*, **543**, A27
- Goicoechea, J. R., Pety, J., Gerin, M., Hily-Blant, P., & Le Bourlot, J. 2009, *A&A*, **498**, 771
- Goodman, A. A., Alves, J., Beaumont, C. N., et al. 2014, *ApJ*, **797**, 53
- Goodman, A. A., Benson, P. J., Fuller, G. A., & Myers, P. C. 1993, *ApJ*, **406**, 528
- Gordon, M. A. 1987, *ApJ*, **316**, 258
- Gordon, M. A., & Burton, W. B. 1976, *ApJ*, **208**, 346
- Griffin, M. J., Abergel, A., Abreu, A., et al. 2010, *A&A*, **518**, L3
- Gutermuth, R. A., & Heyer, M. 2015, *AJ*, **149**, 64
- Guzmán, A. E., May, J., Alvarez, H., & Maeda, K. 2011, *A&A*, **525**, A138
- Haikala, L. K., Harju, J., Mattila, K., & Toriseva, M. 2005, *A&A*, **431**, 149
- Harper-Clark, E., & Murray, N. 2009, *ApJ*, **693**, 1696
- Hartmann, L., Megeath, S. T., Allen, L., et al. 2005, *ApJ*, **629**, 881
- Haslam, C. G. T., Salter, C. J., Stoffel, H., & Wilson, W. E. 1982, *A&AS*, **47**, 1
- He, Y.-X., Zhou, J.-J., Esimbek, J., et al. 2015, *MNRAS*, **450**, 1926
- Henning, T., Linz, H., Krause, O., et al. 2010, *A&A*, **518**, L95
- Henshaw, J. D., Caselli, P., Fontani, F., et al. 2016, *MNRAS*, **463**, 146
- Hoare, M. G., Roche, P. F., & Glencross, W. M. 1991, *MNRAS*, **251**, 584
- Israel, F. P. 1978, *A&A*, **70**, 769
- Jackson, J. M., Finn, S. C., Chambers, E. T., Rathborne, J. M., & Simon, R. 2010, *ApJL*, **719**, L185
- Jackson, J. M., Rathborne, J. M., Foster, J. B., et al. 2013, *PASA*, **30**, e057
- Jiménez-Serra, I., Caselli, P., Fontani, F., et al. 2014, *MNRAS*, **439**, 1996
- Jin, M., Lee, J.-E., Kim, K.-T., & Evans, N. J., II 2016, *ApJS*, **225**, 21
- Kahn, F. D. 1974, *A&A*, **37**, 149
- Kerton, C. R., Arvidsson, K., & Alexander, M. J. 2013, *AJ*, **145**, 78
- Kirk, H., Myers, P. C., Bourke, T. L., et al. 2013, *ApJ*, **766**, 115
- Kobulnicky, H. A., Chick, W. T., Schurhammer, D. P., et al. 2016, *ApJS*, **227**, 18
- Kobulnicky, H. A., & Johnson, K. E. 1999, *ApJ*, **527**, 154
- Kroupa, P. 2001, *MNRAS*, **322**, 231
- Krumholz, M. R., & McKee, C. F. 2008, *Natur*, **451**, 1082
- Kurtz, S., Churchwell, E., & Wood, D. O. S. 1994, *ApJS*, **91**, 659
- Lada, C. J., & Adams, F. C. 1992, *ApJ*, **393**, 278
- Lada, C. J., & Lada, E. A. 2003, *ARA&A*, **41**, 57
- Lada, C. J., Muench, A. A., Luhman, K. L., et al. 2006, *AJ*, **131**, 1574
- Lada, C. J., Muench, A. A., Rathborne, J., Alves, J. F., & Lombardi, M. 2008, *ApJ*, **672**, 410
- Launhardt, R., Stutz, A. M., Schmiedeke, A., et al. 2013, *A&A*, **551**, A98
- Li, G.-X., Urquhart, J. S., Leurini, S., et al. 2016, *A&A*, **591**, A5
- Liu, T., Wu, Y., & Zhang, H. 2013a, *ApJ*, **776**, 29
- Liu, X.-L., Wang, J.-J., & Xu, J.-L. 2013b, *MNRAS*, **431**, 27
- López-Sepulcre, A., Cesaroni, R., & Walmsley, C. M. 2010, *A&A*, **517**, A66
- Mac Low, M.-M., van Buren, D., Wood, D. O. S., & Churchwell, E. 1991, *ApJ*, **369**, 395
- Mardones, D., Myers, P. C., Tafalla, M., et al. 1997, *ApJ*, **489**, 719
- Martin, S. C. 1996, *ApJ*, **473**, 1051
- Megeath, S. T., Allen, L. E., Gutermuth, R. A., et al. 2004, *ApJS*, **154**, 367
- Meyer, M. R., Calvet, N., & Hillenbrand, L. A. 1997, *AJ*, **114**, 288
- Miettinen, O. 2012, *A&A*, **540**, A104
- Miettinen, O. 2014, *A&A*, **562**, A3
- Miettinen, O., & Harju, J. 2010, *A&A*, **520**, A102
- Molinari, S., Swinyard, B., Bally, J., et al. 2010, *PASP*, **122**, 314
- Monet, D. 1998, *USNO-A2.0* (Flagstaff, AZ: United States Naval Observatory)

- Murray, N. 2011, *ApJ*, **729**, 133
- Myers, P. C. 2009, *ApJ*, **700**, 1609
- Nakashima, J.-i., Ladeyschikov, D. A., Sobolev, A. M., et al. 2016, *ApJ*, **825**, 16
- Nandakumar, G., Veena, V. S., Vig, S., et al. 2016, *AJ*, **152**, 146
- Noriega-Crespo, A., Morris, P., Marleau, F. R., et al. 2004, *ApJS*, **154**, 352
- Ochsendorf, B. B., Cox, N. L. J., Krijt, S., et al. 2014, *A&A*, **563**, A65
- Olmon, F. M. 1975, *A&A*, **39**, 217
- Osterbrock, D. E. 1989, *Astrophysics of Gaseous Nebulae and Active Galactic Nuclei* (Mill Valley, CA: Univ. Science Books)
- Panagia, N. 1973, *AJ*, **78**, 929
- Panagia, N., & Felli, M. 1975, *A&A*, **39**, 1
- Perauld, M., Omont, A., Simon, G., et al. 1996, *A&A*, **315**, L165
- Peri, C. S., Benaglia, P., Brookes, D. P., Stevens, I. R., & Isequilla, N. L. 2012, *A&A*, **538**, A108
- Peri, C. S., Benaglia, P., & Isequilla, N. L. 2015, *A&A*, **578**, A45
- Pilbratt, G. L., Riedinger, J. R., Passvogel, T., et al. 2010, *A&A*, **518**, L1
- Poglitsch, A., Waelkens, C., Geis, N., et al. 2010, *A&A*, **518**, L2
- Povich, M. S., Benjamin, R. A., Whitney, B. A., et al. 2008, *ApJ*, **689**, 242
- Purcell, C. R., Balasubramanyam, R., Burton, M. G., et al. 2006, *MNRAS*, **367**, 553
- Quireza, C., Rood, R. T., Bania, T. M., Balser, D. S., & Maciel, W. J. 2006, *ApJ*, **653**, 1226
- Ragan, S. E., Heitsch, F., Bergin, E. A., & Wilner, D. 2012, *ApJ*, **746**, 174
- Ragan, S. E., Henning, T., Tackenberg, J., et al. 2014, *A&A*, **568**, A73
- Rathborne, J. M., Jackson, J. M., & Simon, R. 2006, *ApJ*, **641**, 389
- Redman, M. P., Keto, E., Rawlings, J. M. C., & Williams, D. A. 2004, *MNRAS*, **352**, 1365
- Reynolds, S. P. 1986, *ApJ*, **304**, 713
- Rho, J., Reach, W. T., Lefloch, B., & Fazio, G. G. 2006, *ApJ*, **643**, 965
- Rieke, G. H., & Lebofsky, M. J. 1985, *ApJ*, **288**, 618
- Robitaille, T. P., Whitney, B. A., Indebetouw, R., & Wood, K. 2007, *ApJS*, **169**, 328
- Robitaille, T. P., Whitney, B. A., Indebetouw, R., Wood, K., & Denzmore, P. 2006, *ApJS*, **167**, 256
- Roger, R. S., Costain, C. H., Landecker, T. L., & Swerdlyk, C. M. 1999, *A&AS*, **137**, 7
- Russeil, D., Schneider, N., Anderson, L. D., et al. 2013, *A&A*, **554**, A42
- Rygl, K. L. J., Wyrowski, F., Schuller, F., & Menten, K. M. 2013, *A&A*, **549**, A5
- Sánchez-Monge, Á., Beltrán, M. T., Cesaroni, R., et al. 2013, *A&A*, **550**, A21
- Sanhueza, P., Jackson, J. M., Zhang, Q., et al. 2017, *ApJ*, **841**, 97
- Schisano, E., Rygl, K. L. J., Molinari, S., et al. 2014, *ApJ*, **791**, 27
- Schmiedeke, A., Schilke, P., Möller, T., et al. 2016, *A&A*, **588**, A143
- Schuller, F., Menten, K. M., Contreras, Y., et al. 2009, *A&A*, **504**, 415
- Schutte, A. J., van der Walt, D. J., Gaylard, M. J., & MacLeod, G. C. 1993, *MNRAS*, **261**, 783
- Scoville, N. Z., & Solomon, P. M. 1975, *ApJL*, **199**, L105
- Shetty, R., Kauffmann, J., Schnee, S., & Goodman, A. A. 2009, *ApJ*, **696**, 676
- Shipman, R. F., van der Tak, F. F. S., Wyrowski, F., Herpin, F., & Frieswijk, W. 2014, *A&A*, **570**, A51
- Shull, J. M. 1980, *ApJ*, **238**, 860
- Simpson, R. J., Povich, M. S., Kendrew, S., et al. 2012, *MNRAS*, **424**, 2442
- Smith, R. J., Shetty, R., Beuther, H., Klessen, R. S., & Bonnell, I. A. 2013, *ApJ*, **771**, 24
- Sodroski, T. J. 1991, *ApJ*, **366**, 95
- Sokolov, V., Wang, K., Pineda, J. E., et al. 2017, *A&A*, **606**, A133
- Stahler, S. W., & Palla, F. 2005, *The Formation of Stars*, 865
- Sugitani, K., Tamura, M., Nakajima, Y., et al. 2002, *ApJL*, **565**, L25
- Sun, Y., & Gao, Y. 2009, *MNRAS*, **392**, 170
- Svoboda, B. E., Shirley, Y. L., Battersby, C., et al. 2016, *ApJ*, **822**, 59
- Swarup, G., Ananthakrishnan, S., Kapahi, V. K., et al. 1991, *CSci*, **60**, 95
- Takami, M., Karr, J. L., Koh, H., Chen, H.-H., & Lee, H.-T. 2010, *ApJ*, **720**, 155
- Tan, J. C., Krumholz, M. R., & McKee, C. F. 2006, *ApJL*, **641**, L121
- Tej, A., Ojha, D. K., Ghosh, S. K., et al. 2006, *A&A*, **452**, 203
- Tenorio-Tagle, G. 1979, *A&A*, **71**, 59
- Tobin, J. J., Hartmann, L., Bergin, E., et al. 2012, *ApJ*, **748**, 16
- Treviño-Morales, S. P., Pilleri, P., Fuente, A., et al. 2014, *A&A*, **569**, A19
- Turner, B. E., & Matthews, H. E. 1984, *ApJ*, **277**, 164
- van Buren, D., & Mac Low, M.-M. 1992, *ApJ*, **394**, 534
- Veena, V. S., Vig, S., Tej, A., Kantharia, N. G., & Ghosh, S. K. 2017, *MNRAS*, **465**, 4219
- Walsh, A. J., Hyland, A. R., Robinson, G., & Burton, M. G. 1997, *MNRAS*, **291**, 261
- Wang, K., Testi, L., Burkert, A., et al. 2016, *ApJS*, **226**, 9
- Wang, K., Testi, L., Ginsburg, A., et al. 2015, *MNRAS*, **450**, 4043
- Wang, K., Zhang, Q., Testi, L., et al. 2014, *MNRAS*, **439**, 3275
- Ward-Thompson, D., Kirk, J. M., André, P., et al. 2010, *A&A*, **518**, L92
- Ward-Thompson, D., & Robson, E. I. 1990, *MNRAS*, **244**, 458
- Watson, C., Corn, T., Churchwell, E. B., et al. 2009, *ApJ*, **694**, 546
- Watson, C., Povich, M. S., Churchwell, E. B., et al. 2008, *ApJ*, **681**, 1341
- Weaver, R., McCray, R., Castor, J., Shapiro, P., & Moore, R. 1977, *ApJ*, **218**, 377
- Wilkin, F. P. 1996, *ApJL*, **459**, L31
- Wilkin, F. P. 2000, *ApJ*, **532**, 400
- Wood, D. O. S., & Churchwell, E. 1989, *ApJS*, **69**, 831
- Xu, J.-L., Li, D., Zhang, C.-P., et al. 2016, *ApJ*, **819**, 117
- Xu, J.-L., Xu, Y., Zhang, C.-P., et al. 2017, *A&A*, in press (arXiv:1708.09098)
- Yu, N.-P., & Wang, J.-J. 2013, *RAA*, **13**, 28
- Zhang, C.-P., Yuan, J.-H., Li, G.-X., Zhou, J.-J., & Wang, J.-J. 2017, *A&A*, **598**, A76
- Zinnecker, H., & Yorke, H. W. 2007, *ARA&A*, **45**, 481
- Zucker, C., Battersby, C., & Goodman, A. 2015, *ApJ*, **815**, 23